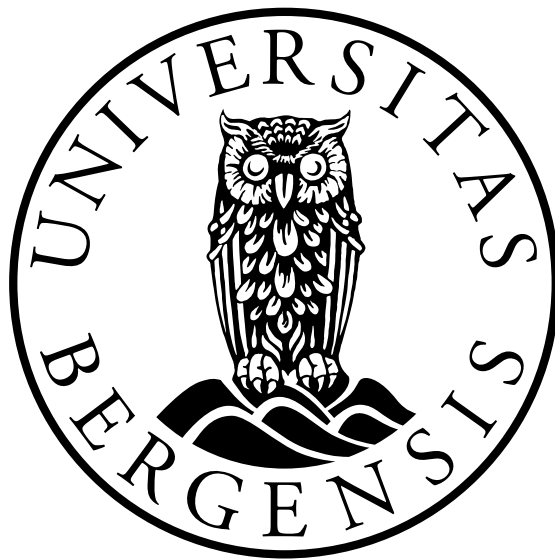


Analysis of DCE-MRI data from patients with endometrial cancer

Ingrid Aase Cowles



Master's Thesis in Medical Technology
Department of physics and technology
University of Bergen

June 2023

Scientific environment

This study was carried out at the Department of Physics and Technology, University of Bergen, in collaboration with Mohn Medical Imaging and Visualization Centre (MMIV), the Department of Radiology at Haukeland University Hospital (HUS), the Department of Clinical Engineering at HUS, Kvinneklubben at HUS and the Department of Computer science, Electrical engineering and Mathematical sciences, Western Norway University of Applied Sciences.

Acknowledgements

Initially, I would like to thank my supervisor Erlend Hodneland for handing me an exciting project. You have been highly investigated in the project and available for all questions over the past two years. Thank you for sharing all of your knowledge and ideas and for inspiring and supporting me during this project.

I would also like to thank my co-supervisor Erik A. Hanson for sharing your knowledge and ideas. Your insights and feedback have been very valuable. Also, I would like to express my gratitude to Erling Andersen for creating the Python library used for image analysis in this project and for providing support, feedback and knowledge. Thank you, Zhanbolat Satybaldinov and Hauke Bartsch for helping me implement this project into the research information system and always being available to help.

Thank you to everyone at MMIV for warmly welcoming me. Especially, thank you Ingrid Haldorsen for sharing your wisdom and for making me a part of the Cancer imaging group at MMIV and Kvinneklubben, headed by Ingrid and Camilla Krakstad. I have truly learned a lot from the members of this group. I am grateful for the chance to present a poster of my project at the MMIV conference and for the opportunity to attend the seminar in Voss alongside the research group. These experiences have been invaluable in terms of my learning and growth. Thank you to Erlend and Ingrid for making it all possible. I would like to thank Kristine Fasmer, Kari Wagner-Larsen and Julie Andrea Dybvik for generously sharing your knowledge on the research field.

I would like to express my thankfulness to my friends and family for always supporting me. A big thank you goes out to all my study friends for their generous contributions of knowledge, kindness, and for creating a highly positive learning atmosphere.

Ingrid Aase Cowles
Bergen, June 2023

Abstract

Purpose: The purpose of this thesis is to find quantitative perfusion parameters from dynamic contrast-enhanced magnetic resonance imaging (DCE-MRI) time-series data that might be related to tumor biology in endometrial cancer.

Methods: The pharmacokinetic model extended Tofts' method (ETM) was used to derive quantitative perfusion parameters. Two different environments were used for modeling. The research information system was utilized to test ETM on data from n=63 patients. A population-based arterial input function (AIF) was used when modeling in the research environment. Two other methods for estimating the AIF, including manual annotation and a semi-automatic algorithm were implemented in a local modeling environment and tested on data from n=20 patients. Correlations between the derived parameters and low-risk and high-risk histologic tumor grades were examined.

Results: Modeling based on the voxelwise signal intensity gave slightly higher K^{trans} values than modeling based on the average signal intensity for all AIF methods. The semi-automatic AIF method exhibits larger mean model parameters from ETM than the two other AIF methodologies, even though the median K^{trans} values are in line with the two other AIF methods. Outliers were observed in the derived model parameters from ETM when the semi-automatic algorithm was used for estimating the AIF. ROC curves of the model parameters and histologic tumor grade show no correlation between the parameters derived from ETM and histologic tumor grade in this project.

Conclusion: Modeling based on the average signal intensity inside the tumor exhibits higher consistency in the derived model parameters than modeling based on the voxelwise signal intensity inside the tumor. The AIF affects the derived model parameters a lot. The population-based AIF method was evaluated as the most robust method for estimating the AIF in this project. We found no correlation between the derived perfusion parameters and histologic tumor grade.

Contents

Scientific environment	i
Acknowledgements	iii
Abstract	v
Abbreviations and symbols	xiii
1 Introduction	1
1.1 Tissue and imaging biomarkers in endometrial cancer	3
1.2 Preoperative imaging with DCE-MRI	4
1.3 Motivation, purpose and objectives	4
2 Theory	7
2.1 Principles of DCE-MRI	7
2.1.1 Magnetic resonance imaging	7
2.1.2 Dynamic contrast-enhanced MRI	8
2.2 Pharmacokinetic modeling	10
2.2.1 Extended Tofts' method	11
2.3 Heuristic methods	13

2.4	The Arterial Input function	14
2.4.1	Manual annotation of the AIF	15
2.4.2	Automatic algorithm for detecting the AIF	15
2.4.3	Population-based AIF	16
2.5	Imaging systems and information flow	17
2.6	Statistical evaluation	18
3	Materials and methods	23
3.1	Patient data	23
3.2	Imaging protocol	24
3.3	Tumor segmentations	24
3.4	The arterial input function	24
3.4.1	Manual annotation of the AIF	25
3.4.2	Semi-automatic algorithm for detecting the AIF	25
3.4.3	Population-based AIF	26
3.5	Extended Tofts' method	26
3.5.1	Analytical solution	26
3.5.2	Python implementation	27
3.6	Integration into the research information system	29
3.7	Evaluation	30
3.7.1	Evaluating results from the local environment	30
3.7.2	Evaluating results from the research environment	31
3.7.3	Statistical considerations	32

4	Results	33
4.1	The arterial input function	33
4.1.1	Manually annotated AIF	33
4.1.2	Semi-automatic AIF algorithm	34
4.1.3	Population-based AIF	36
4.2	Extended Tofts' method	36
4.2.1	Local modeling environment	37
4.2.2	Modeling in the research information system	47
4.3	Correlation with histologic tumor grade	49
5	Discussion	51
5.1	The Arterial Input function	51
5.1.1	The manually annotated AIF	52
5.1.2	The semi-automatic AIF	53
5.1.3	The population-based AIF	54
5.2	Extended Tofts' Method	54
5.2.1	Comparing average and voxelwise modeling results	55
5.2.2	Modeling results from different AIF methods	57
5.2.3	Erosion and dilation of tumor masks	59
5.2.4	Parameter maps	59
5.2.5	Comparison with values from the literature	60
5.2.6	Correlation with histologic tumor grade	62
5.3	Future work	63

6	Conclusions	65
	Source code	66
A	Extended Tofts' model	69
A.1	Analytical solution to ETM	69
A.2	Model parameters obtained from ETM	70
A.2.1	Manual AIF	71
A.2.2	Population-based AIF	72
A.2.3	Semi-automatic AIF	74
A.3	Statistical evaluation	78
A.3.1	Spearman's rank correlation coefficient	78
A.3.2	Wilcoxon signed-rank test	78
B	The arterial input function	81
B.1	Cost values from the semi-automatic AIF	81

Abbreviations and symbols

Abbreviations

AIF	Arterial input function
AUC	Area under curve
CA	Contrast agent
DCE-MRI	Dynamic contrast-enhanced magnetic resonance imaging
CI	Confidence interval
CNN	Convolutional neural network
DICOM	Digital imaging and communications in medicine
EES	Extravascular extracellular space
ETM	Extended Tofts' method
FA	Flip angle
FIGO	Surgical International Federation of Gynecology and Obstetrics
FN	False negatives
FPR	False positive rate
Gd	Gadolinium
Hct	Hematocrit
HUS	Haukeland University Hospital
MRI	Magnetic resonance imaging
MMIV	Mohn medical imaging and visualization centre
RF	Radio frequency
ROC	Receiver operating characteristics
ROI	Region of interest
PACS	Picture archiving and communication system
PCC	Pearson correlation coefficient
PE	Peak enhancement
PET	Position emission tomography
PS	Permeability surface area product
TE	Echo time
TM	Tofts method
TR	Repetition time
TP	True positives
TPR	True positive rate
TTP	Time to peak
VIBE	Volumetric interpolated breath-hold examination

Symbols

α	Significance level of statistical tests
θ	Flip angle (FA)
\mathbf{B}_0	Main magnet field
$C_b(t)$	Blood concentration
$C_e(t)$	EES concentration
$C_p(t)$	Plasma concentration
$C_t(t)$	Total tissue concentration
K^{trans}	Transfer constant describing the transfer of CA from plasma to EES
k_{ep}	Transfer constant describing the transfer of CA from EES to plasma
R_1	Relaxation rate
r_1	Relaxivity
S	MRI signal intensity
S_0	MRI signal intensity before injection of CA
T_1	The time at which the magnetization is regained along the longitudinal direction
T_{10}	Value of T_1 before injection of CA
T_2	The time at which the magnetization is lost in the transversal plane
T1W	T_1 -weighted
T2W	T_2 -weighted
t	Time
v_e	Fractional volume of EES
v_p	Fractional volume of plasma

List of Figures

- 1.1 The anatomy of the uterus including an explanation of the different FIGO stages (Images from [8]). 2

- 2.1 An illustration of the parameters in extended Tofts' method. The light blue area is the extravascular extracellular space (EES), while the dark blue space is the intracellular space. The blood vessel contains plasma and red blood cells. The small grey dots in the plasma and in the EES illustrates Gadolinium (Gd). $K^{trans}(min^{-1})$ and $k_{ep}(min^{-1})$ are transfer constants, characterizing the transfer of Gd across the endothelium. The relative sizes are not correct in this figure. (illustration inspired by [23]). 12

- 2.2 An illustration of the parameters peak enhancement (PE) and time-to-peak (TTP), which can be estimated by heuristic methods. 14

- 2.3 The kinetics of the arterial input function (AIF). 15

- 4.1 DCE-MRI images from two different patients showing the placement of regions of interest of the arterial input function (AIF) and the corresponding AIF curves. The left AIF curve corresponds to the left image, while the right AIF curve corresponds to the right image. More noise and a lower peak value are illustrated in the right AIF curve. 34

- 4.2 Arterial input function (AIF) curves estimated from the semi-automatic AIF algorithm. The left AIF curve is based on the same patient data as the manually segmented AIF curve illustrated to the left in figure 4.1. The right AIF curve is based on the same patient data as the manually segmented AIF curve illustrated to the right in figure 4.1. The left curve looks like the desired AIF curve, while the right curve seems to be noise with no distinct peak value. 35
- 4.3 The population-based arterial input function, which was calculated based on manually annotated AIF data from 20 patients. 36
- 4.4 The absolute differences in K^{trans} derived from extended Tofts' method when modeling based on the average signal intensity and from modeling based on the voxelwise signal intensity inside a tumor. Four different methods were used for estimating the arterial input function (AIF). The y-axis of the different plots are of different ranges, illustrating differences between the derived K^{trans} values when using different AIF methods. 38
- 4.5 Bland-Altman plots of the derived K^{trans} values from extended Tofts' method using four different methods for finding the arterial input function (AIF). The difference between the derived K^{trans} values from average and voxelwise modeling are here analyzed. $+LoA$ and $-LoA$ show the upper and lower limits of agreement, respectively. The y-axis range differs between the plots. Small bias is observed for all AIF methods. . . 39
- 4.6 The absolute differences between the derived k_{ep} values from extended Tofts' model when modeling based on the average signal intensity and modeling based on the voxelwise signal intensity inside the tumor. The values are plotted against the tumor volume. The y-axis range differs in the four plots. 40
- 4.7 Bland-Altman plots of the derived K^{trans} values from extended Tofts' method, comparing three different arterial input function (AIF) methods, illustrating that the semi-automatic AIF approach results in more outliers in the derived K^{trans} values. The axes of the plots have different ranges and LoA represents the upper and lower limits of agreement. . . 42

- 4.8 The tissue signal intensity estimated by extended Tofts' method plotted together with the mean signal intensity inside the tumor and the plasma signal intensity. In the plots, the raw signal illustrates the signal intensity curves in the tissue of interest before modeling. The plots are based on data from two different patients. All of the plots to the right are based on the same patient data, while the plots to the left are based on the same patient data. 44
- 4.9 Parameter maps of the parameters K^{trans} , k_{ep} , v_e and v_p derived from extended Tofts' method when using a manually annotated arterial input function. v_e and v_p are fractions of the total tissue volume inside a voxel. 46
- 4.10 Differences in $K^{trans}(min^{-1})$ values from Extended Tofts' model when modeling based on the average signal intensity and modeling based on the voxelwise signal intensity inside the tumor (n=63). No specific coherence seems to be present between the K^{trans} differences and tumor volumes. 48
- 4.11 Bland-Altman plot of the K^{trans} parameters from extended Tofts' method, illustrating the differences between the derived K^{trans} values when modeling based on the average signal intensity and modeling based on the voxelwise signal intensity inside the tumor (n=63). A population-based arterial input function was used. +LoA and -LoA represent the upper and lower limits of agreement. 48
- 4.12 Receiver operating characteristics (ROC) curves, where it is analyzed whether there is a correlation between the derived model parameters and histologic tumor grade (n=60). The histologic tumor grade is divided into low-risk and high-risk tumor grades. No correlation is observed from this figure. 50

List of Tables

4.1	Mean model parameters and standard deviations from extended Tofts' method when using different methods for estimating the arterial input function (AIF). v_e and v_p are fractions of the total tissue volume inside a voxel, K^{trans} and k_{ep} have the unit min^{-1} . The absolute mean difference is also included. Higher mean values and absolute mean differences are observed for the semi-automatic AIF methods. 2% and 3% are the portions of bright voxels for the semi-automatic AIF.	37
4.2	A summary of the absolute mean differences in the parameters derived from extended Tofts' method when different methods for estimating the arterial input function were used. K^{trans} and k_{ep} have the unit min^{-1} , while v_e and v_p are fractions of total tissue volume inside a voxel. The percent wise differences are included in parentheses.	41
4.3	A summary of the median K^{trans} , k_{ep} , v_e and v_p derived from extended Tofts' method when using different methods for estimating the arterial input function. The range of the values are included in parenthesis. K^{trans} and k_{ep} have the unit min^{-1} , while v_e and v_p are fractions of total tissue volume inside a voxel.	41
4.4	Median of the derived parameters from extended Tofts' method when using a population-based arterial input function and doing an erosion and a dilation of the tumor masks (n=20). v_e and v_p are fractions of the total tissue volume inside a voxel, while K^{trans} and k_{ep} are in units of min^{-1}	45

4.5	A summary of the mean parameters from extended Tofts' method when using a population-based AIF (n=63). The differences between the results from average and voxelwise modeling are included in the bottom row. v_e and v_p are fractions of the total tissue volume inside a voxel, while K^{trans} and k_{ep} are rates in min^{-1}	47
4.6	The median model parameters from extended Tofts' method when using a population-based AIF (n=63). Only the parameters derived from modeling based on the average signal intensity inside the tumor are included. K^{trans} and k_{ep} have the unit min^{-1} , while v_e and v_p are fractions of total tissue volume inside a voxel.	47
4.7	The median of the derived parameters from extended Tofts' method summarized for low-risk and high-risk histologic tumor grade. The range of the values is added in parentheses. v_e and v_p are fractions of total tissue volume inside a voxel, while K^{trans} and k_{ep} are in units of min^{-1}	49
A.1	Model parameters from extended Tofts' method when using manually annotated arterial input functions and modeling based on the average signal intensity inside the tumor (n=20).	71
A.2	Model parameters from extended Tofts' method when using manually annotated arterial input functions and modeling based on the voxelwise signal intensity inside the tumor(n=20).	71
A.3	Model parameters derived from extended Tofts' method when using a population-based arterial input function and modeling based on the average signal intensity inside the tumor (n=20).	72
A.4	Table showing all the optimized parameters from extended Tofts' method when using a population-based arterial input function and modeling based on the voxelwise signal intensity inside the tumor (n=20).	72

A.5	Model parameters derived from extended Tofts' method when using a population-based arterial input function and an eroded tumor mask (n=20). Modeling was performed based on the average signal intensity inside the tumor.	73
A.6	Model parameters derived from extended Tofts' method when using a population-based arterial input function and a dilated tumor mask (n=20). Modeling was based on the average signal intensity inside the tumor.	73
A.7	Model parameters derived from extended Tofts' method when using a semi-automatic arterial input function, choosing 2% bright voxels and modeling based on the average signal intensity inside the tumor (n=13).	74
A.8	Model parameters derived from extended Tofts' method when using a semi-automatic arterial input function, choosing 2% bright voxels and modeling based on the voxelwise signal intensity inside the tumor (n=13).	74
A.9	Model parameters from extended Tofts' method when using a semi-automatic arterial input function, choosing 3% bright voxels and modeling based on the average signal intensity inside the tumor (n=18). . . .	75
A.10	Model parameters derived from extended Tofts' model when using a semi-automatic arterial input function, choosing 3% bright voxels and modeling based on the voxelwise signal intensity inside the tumor (n=18).	75
A.11	Model parameters derived from extended Tofts' model when using a population-based arterial input function (n=60).	76
A.12	Model parameters derived from extended Tofts' method when using a population-based arterial input function (n=60).	77
A.13	Spearman correlation coefficients and p-values for all of the AIF methodologies when comparing average and voxelwise modeling results. The bottom row shows the correlation coefficient obtained from modeling in the research environment, while the rest of the coefficients were obtained from the local modeling environment.	78

- A.14 Spearman correlation coefficients and p-values for the derived K^{trans} values from the three different methods for estimating the AIF. 78
- A.15 p-values for the derived K^{trans} values from modeling based on the average signal intensity and from modeling based in the voxelwise signal intensity. The bottom row shows the p-value for the model parameters obtained from the research environment, while the rest of the values are based on results from the local modeling environment. Only the population-based method exhibits similar median values from modeling based on the average signal intensity and modeling based on the voxelwise signal intensity. 78
- A.16 p-values for the derived K^{trans} values from the three different methods for estimating the AIF when testing the null hypothesis by the Wilcoxon signed-rank test. 79
- B.1 Cost values for different percentages of bright voxels, 2% and 3% bright voxels. The cost values are based on how well a Parker AIF fits the derived derived AIF from the semi-automatic algorithm. In this table "-" illustrates that the algorithm did not find an AIF for this patient. 81

Chapter 1

Introduction

Endometrial cancer is the most common pelvic gynecological malignancy in Western countries, and the occurrence is increasing [1]. It is the fifth most common cancer type among women in Norway. The occurrence of endometrial cancer increases with increasing age and is most frequently discovered in individuals that are over 60 years old [2].

The endometrium is the inner layer of the uterus. Endometrial cancer (also called endometrial carcinoma) starts in the cells of the inner lining of the uterus (the endometrium) and is the most common type of cancer in the uterus [3]. Endometrial cancer is graded based on how much the cancer cells are organized into glands. Grades 1 and 2 are lower-grade cancer; in these grades, more cancer cells form glands. In grade 3, a higher grade cancer, more cancer cells are disorganized and do not form glands. Grade 3 endometrial cancer tends to grow and spread faster than cancer of grades 1 and 2. In addition, grade 3 cancers have a poorer outlook than endometrial cancers of lower grade [4][5].

The histologic types of endometrial carcinomas are defined based on how the cancer cells look when they are investigated under a microscope. Histologic types of endometrial cancer include adenocarcinoma, uterine carcinosarcoma, squamous cell carcinoma, small cell carcinoma, transitional carcinoma and serous carcinoma. The majority of endometrial cancers are a type of adenocarcinoma called endometrioid cancer [4].

In addition to grade and histological type, treatment and prognosis are influenced by the surgical International Federation of Gynecology and Obstetrics (FIGO) staging system

[1]. The FIGO stage is important when deciding how to treat endometrial cancer. The FIGO system stages endometrial cancer based on the extent of the tumor, the spread to nearby lymph nodes, and metastasis [6][7]. Figure 1.1 shows some of the different FIGO stages of endometrial cancer.

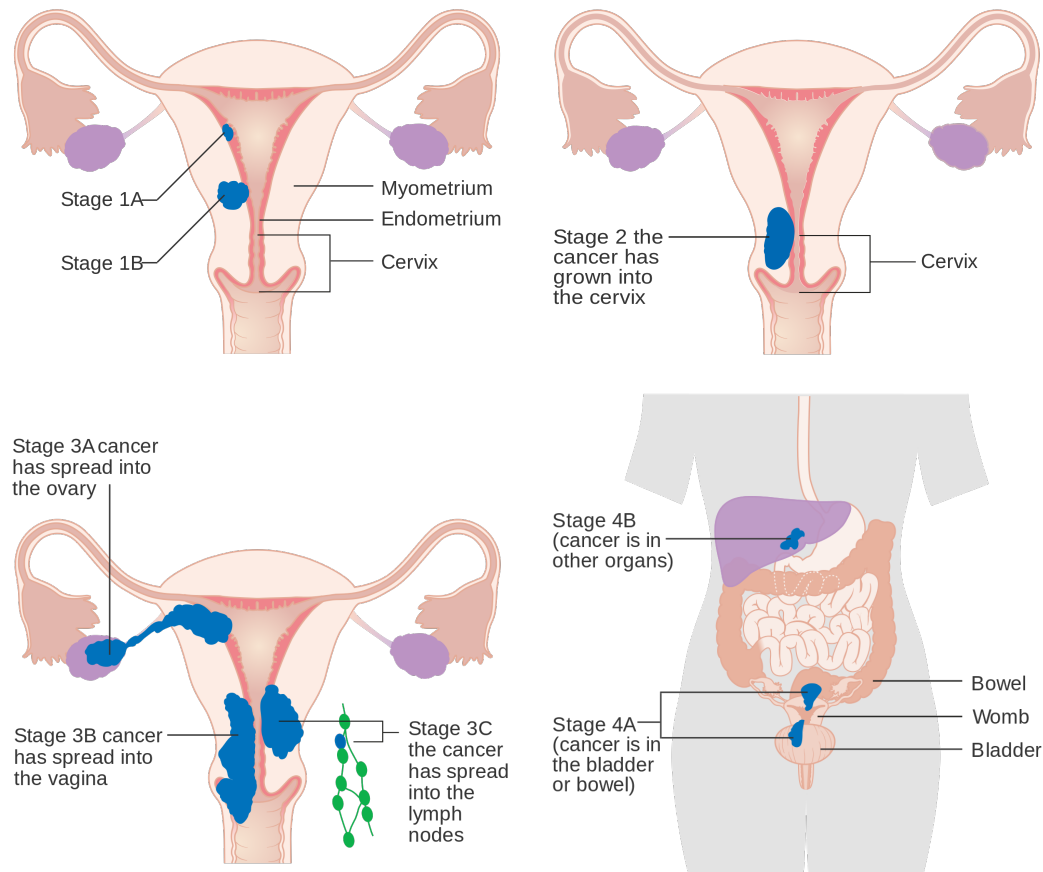


Figure 1.1: The anatomy of the uterus including an explanation of the different FIGO stages (Images from [8]).

Certain factors increase the risk of developing endometrial cancer. These include, among other things, heredity, obesity, type 2 diabetes, never having had a child, late menopause, increasing age and high levels of estrogen [2][6]. Lifestyle can influence the risk of developing endometrial cancer. The reason behind endometrial cancer is mostly unknown, even though there are some known risk factors that can influence the risk of developing endometrial cancer [2].

The five-year overall survival for FIGO stage I and II endometrial cancer is 74% – 91%. FIGO stage III endometrial cancer has a five-year overall survival of 57% – 66%, while the five-year overall survival for FIGO stage IV is 20% – 26%. Patients with pelvic lymph node metastasis have a five-year disease-free survival of 60% – 70%,

while patients without lymph node metastasis have a five-year disease-free survival of about 90%. About 75% of endometrial cancer cases are diagnosed early at FIGO stages I or II. A considerable portion of endometrial cancer patients dies from other health conditions and not from endometrial cancer because these patients often have several comorbidities. In addition to FIGO stage, survival is dependent on other predictive factors, such as tumor grade, tumor diameter, age, and comorbidities [6].

The standard treatment for apparent FIGO stage I endometrial cancer is hysterectomy and removal of the ovaries and the uterine tubes. This can be done using techniques that are minimally invasive. The practice for patients with lymph node metastasis varies worldwide [6]. In Norway, surgery is the most common way of treating endometrial cancer. Radiation therapy or chemotherapy is sometimes given to patients in Norway when surgery is advised against [2].

The symptoms of endometrial cancer include bleeding from the vagina after menopause, an unusual amount of discharge, and new pelvic pain. If there is suspicion of endometrial cancer a gynecological examination will be executed, where a sample will be taken from the uterus. A CT scan is acquired to find out if the cancer is metastatic. In addition, an MRI scan is acquired to see if the cancer has spread outside the endometrium [2]. Dynamic contrast-enhanced MRI (DCE-MRI) has the potential to give us additional information about the tumor, which might help with diagnosis, and hence, might result in a better treatment [1].

1.1 Tissue and imaging biomarkers in endometrial cancer

There are certain biomarkers that are relevant for diagnosis, treatment planning and response to therapy in endometrial cancer. Biomarkers for endometrial cancer include histologic information, which can be found from gynecological investigations and biopsies, in addition to information regarding metastasis, infiltration of the myometrium and cervix and size of the tumor, which can be found from MRI [9]. Oncogenes, cancer suppressor genes and several other genes and molecules have been identified as endometrial cancer biomarkers [9].

MRI and especially contrast-enhanced MRI is used for detecting myometrial invasion, cervical invasion, and lymph node metastasis. Imaging techniques generally have poor detection of lymph node metastasis, which is the major limitation. For detection of

myometrial and cervical invasion and lymph node metastasis 18F-fluorodeoxyglucose PET-CT has shown high accuracy for advanced-stage endometrial cancer [6]. Imaging biomarkers are important and quantitative DCE-MRI may yield parameters relevant for treatment planning and response to therapy [1].

1.2 Preoperative imaging with DCE-MRI

Pelvic MRI is established as a valuable imaging method in the preoperative staging of endometrial cancer. Preoperative staging is important for determining risk groups for recurrence. This is primarily achieved by examining lymph node metastasis, myometrial invasion, and cervical invasion to inform surgical management decisions [6]. In addition to structural MRI, contrast-enhanced MRI with an intravenously injected contrast agent (CA) is commonly acquired due to its diagnostic performance in identifying deep myometrial invasion compared to non-contrast MRI. For diagnosing deep myometrial invasion the optimal contrast timing is approximately 2 minutes post-injection of CA. Then, tumor tissue and the outer myometrial muscular layer can be discriminated. However, even though MRI is considered one of the best imaging modalities for preoperative staging in endometrial cancer, contrast-enhanced MRI is still somewhat variable in diagnostic performance [10].

A few earlier studies have suggested a link between derived pharmacokinetic parameters and high-risk endometrial cancer [1][11][12][13]. There might be a potential to use DCE-MRI as a tool for early diagnosis and prediction of treatment response in endometrial cancer. One of the most frequently used pharmacokinetic models is the extended Tofts' Method (ETM) [14]. In order to implement this model an arterial input function (AIF) is required, which is the input concentration of a CA into the tissue of interest [15].

1.3 Motivation, purpose and objectives

The purpose of this master thesis is to investigate DCE-MRI data from patients diagnosed with endometrial cancer and to discover quantitative perfusion parameters that might be associated with tumor biology. Exploration of the differences between modeling based on the average signal intensity inside the tumor and modeling based on the

voxelwise signal intensity might give an opportunity to discuss the validity of ETM on voxels.

An AIF is required in order to extract model parameters from ETM. Different methods for estimating the AIF will be implemented and tested to see how the AIF affects the parameters derived from ETM. Furthermore, it does not seem to be an apparent indication as to which method is the most effective or optimal for estimating the AIF. There are also practical challenges associated with the task of estimating the AIF, which will be explored and addressed in this thesis.

In order to compare different methodologies and analyze results it is important to have access to a larger number of data. This aspect is also important when examining correlations between the resulting model parameters and clinical parameters. A larger number of data can be found in Sectra research PACS. By utilizing the research information system at Mohn Medical Imaging and Visualization (MMIV) Center and the Radiology Department at Haukeland University Hospital (HUS), perfusion parameters can be derived from a broader range of data. The main objectives of this thesis are:

- (I) Implement ETM in the research information system and optimize perfusion parameters for a larger number of endometrial cancer patients.
- (II) Test ETM for both the average CA concentration inside the tumor and for voxelwise CA concentration inside the tumor and compare the results.
- (III) Implement different methods for estimating the AIF, including manual annotation on DCE-MRI images, automatic detection of the AIF using an algorithm and a population-based AIF.
- (IV) Compare the model parameters derived from ETM with values from the literature and check for correlations with clinical parameters.

Chapter 2

Theory

This chapter includes theory regarding the principles of DCE-MRI and pharmacokinetic modeling, with a special emphasis on the extended Tofts' method (ETM), which is the model used in this project. Theory regarding three different methods for estimating the arterial input function (AIF) is also presented in this chapter, as well as imaging systems used in medical imaging generally and in this project. At the end of this chapter, theory regarding methods for statistically evaluating modeling results is presented.

2.1 Principles of DCE-MRI

2.1.1 Magnetic resonance imaging

Magnetic resonance imaging (MRI) plays an important role in the detection and disease evaluation of endometrial cancer. MRI exploits that the body is made up of 60 – 80% water. Water contains protons which have a net magnetization. MRI is based on the fact that particles like protons have spin. The proton acts like a magnet. If we apply a very strong external magnetic field (1-7 Tesla) the protons in the body of the patient will align with or against the external magnetic field. The protons can then absorb radio frequency (RF) waves and reemit this RF energy. The time at which the protons reemit the RF energy is dependent on the magnetic properties of the tissue. Most diseases lead to changes in the fluid content of the chemical environment of the tissue, therefore MRI is very sensitive to pathological changes, such as tumors [16].

Three parameters for manipulating image contrast from MRI are particularly relevant. The flip angle (FA) is the angle between the magnetization vector and its equilibrium position along the main magnetic field (\mathbf{B}_0) immediately after absorption of an RF pulse. The echo time (TE) is the time from the excitation of a tissue to the readout of the signal and the repetition time (TR) is the time between two RF pulses [16].

The quality of an MRI image is influenced by several factors. The signal-to-noise ratio (SNR) and the contrast between tissues affect the resulting quality of an MRI image. SNR is determined by dividing the average signal intensity within a specific ROI in the object being imaged by the standard deviation in an ROI outside the object being imaged. The temporal and spatial resolution also affect the quality of an MRI image. The spatial resolution is related to the number of pixels in the MRI image, while the temporal resolution is related to the time during the acquisition of a single frame in the dynamic images [16].

There are some tissue specific properties in MRI, including the time constants T_1 and T_2 . These two constants describe the relaxation process in MRI and they are dependent on the composition and structure of the tissue being imaged, as well as the surrounding tissues. T_1 -weighted (T1W) and T_2 -weighted (T2W) MRI images are typically acquired in the clinic. This means that the T_1 or T_2 relaxation process is weighted, while actually, all relaxation processes are present at all times while acquiring an MRI image. In T1W imaging it is the T_1 -relaxation process that is emphasized and T_1 relaxation describes the time at which the magnetization is regained along the longitudinal direction. T_2 relaxation describes the time at which the magnetization is lost in the transversal plane [16].

2.1.2 Dynamic contrast-enhanced MRI

Dynamic contrast-enhanced (DCE) MRI enables us to characterize the tissue microvasculature. By analyzing the leakage of a paramagnetic contrast agent (CA) from the capillaries into the extravascular extracellular space (EES), we can possibly assess quantifiable physiological parameters that might reflect properties of the tissue being imaged [17]. DCE-MRI has been shown to identify biomarkers relevant for treatment response and survival in patients with cervical cancer. It also holds potential for identifying similar biomarkers in patients with endometrial cancer [1].

Following the introduction of a CA into the vascular system, DCE-MRI can be used to analyze the temporal enhancement of the tissue. This is achieved by first acquiring baseline images without CA and then acquiring a series of images over time, usually over a few minutes during and after the injection of CA. The acquired MRI signal can then be used to generate a time-intensity curve for the tissue. This curve shows the tissue's response to the arrival of CA as the concentration of CA over time. By analyzing this curve physiological parameters that might be related to the tissue of interest, can be derived. Such parameters include tissue perfusion, vascular permeability and tissue volume fractions [17].

In DCE-MRI acquisition, repeated T1W images are acquired for several frames before the injection of CA. After the injection of CA, T1W measurements are often acquired. The most widely used CA in MRI, including DCE-MRI, is Gadolinium (Gd). The CA is injected into the bolus with a saline flush after the injection of Gd. Frequently, there is a need to compromise between coverage, temporal resolution, and spatial resolution. Newer scanners have faster gradients, which allows for shorter TR and by using multi-array receiver coils, a higher SNR can be achieved. The optimal DCE-MRI sequence will depend on the organ being measured. Frame times of 2-20 s can be achieved by using spoiled gradient echo methods [18].

To provide an AIF for modeling, the blood signal curve can be measured. To measure the blood signal curve a low temporal resolution of $\sim 3s$ or less is desired. When imaging organs or tumors in the abdomen the aorta is often used as an AIF. For pelvic regions, the iliac arteries can be used as an AIF. For organs located in areas in the body where it can be challenging to identify an adequate AIF, other alternatives like a concentration-time curve in a draining vein or a population AIF can be used [18].

To determine the tissue of interest, it is often necessary to do some kind of segmentation of the tissue of interest. Tumor segmentations can for instance be performed on a single slice or on whole-volume data. For DCE-MRI images it might be convenient to do annotations of the tumor directly on the DCE-MRI images to avoid artefacts due to co-registration between the dynamic and the structural MRI images [1]. Tumor segmentations are still mostly carried out by radiologists, but there is an increasing interest in and development of automatic segmentation methods using deep learning and convolutional neural networks (CNN). Manual segmentation is labor intensive, and whole-volume segmentations are especially time-consuming since annotations are

performed on several slices to cover the whole tumor volume. Automatic methods for the segmentation of tumors in endometrial cancer would most likely enlighten the work of radiologists. An automatic method for the detection and delineation of 3D primary tumors in endometrial cancer was developed by Hodneland et al. using 3D CNNs [19].

2.2 Pharmacokinetic modeling

Parameters reflecting physiology can be derived from pharmacokinetic models, which are models used for analyzing how a drug distributes in the body [20]. When the CA Gd is present, T_1 is reduced from T_{10} , as shown in equation (2.1). T_{10} is the value of T_1 before injection of Gd and $C_t(t)$ is the concentration-time curve in the tissue of interest. r_1 is the relaxivity, which is a constant of proportionality between the Gadolinium concentration and the increase in relaxation rate [21]. r_1 is specific to a contrast agent and varies with field strength [18]. Relaxation rate can be more convenient to use, as shown in equation (2.2), where $R_1 = 1/T_1$ [18].

$$\frac{1}{T_1} = \frac{1}{T_{10}} + r_1 C_t(t) \quad (2.1)$$

$$R_1 = R_{10} + r_1 C_t(t) \quad (2.2)$$

T_1 reduction increases the MRI signal S as shown in equation (2.3). A commonly used technique for quantifying the signal enhancement resulting from the administration of a Gd-based CA is a simple spoiled gradient echo sequence. A simple spoiled gradient echo ("FLASH" or "GRE") sequence is chosen due to its combination of good volume coverage, acceptable precision and accuracy, and acceptable spatial resolution, in addition to acceptable acquisition speed. S_0 is the relaxed signal, which can be found by measuring the MRI signal intensity before the injection of CA. S_0 is equal to S when $TR \gg T_1$ and $\theta = 90^\circ$, where θ is the FA [18].

$$S = S_0 \frac{(1 - e^{-TR/T_1}) \sin \theta}{1 - e^{-TR/T_1} \cos \theta} \quad (2.3)$$

The CA is only present in the plasma of the blood vessels. The plasma concentration, C_p , can be found from the blood concentration, C_b , by adjusting for the hematocrit (Hct), which is the volume percentage of red blood cells in the blood. The blood

concentration is found from the blood signal. The plasma concentration can then be calculated as in equation (2.4). Hct is typically 42% [21][14].

$$C_p(t) = \frac{C_b(t)}{1 - Hct} \quad (2.4)$$

The total tissue concentration is defined in equation (2.5). This equation is valid for a two-compartment model, where the two compartments are plasma and EES, with fractional volumes v_p and v_e , respectively [22]. Compartmental models describe the exchange of CA within a compartment [14]. In equation (2.5) C_e is the concentration of CA in the EES.

$$C_t(t) = C_p(t)v_p + C_e(t)v_e \quad (2.5)$$

ETM is a simple two-compartment model consisting of one tissue compartment and a vascular compartment [14]. The injected CA gives a time-varying blood plasma concentration C_p , and since these contrast agents usually are very small ($< \approx 1000$ daltons), the leakage from the capillaries into the EES is accepted to be diffusive and reversible [18]. The leakage across the endothelium is therefore considered to be proportional to the difference between the concentration in the plasma and the concentration in the EES as illustrated in equation (2.6) [18][21]. In equation (2.6) K^{trans} is a transfer constant.

$$v_e \frac{dC_e(t)}{dt} = K^{trans}(C_p(t) - C_e(t)). \quad (2.6)$$

The solution to equation (2.6) gives the concentration-time curve $C_t(t)$ in the tissue of interest and is known as the extended Tofts' method (ETM).

2.2.1 Extended Tofts' method

ETM is a standard method for analyzing DCE-MRI data. The method was proposed by Paul S. Tofts by pharmacokinetic analysis of the concentration of Gd found from MRI signals [21]. Figure 2.1 gives an illustration of some of the parameters that are included in the model. In ETM each voxel of tissue is assumed to contain three components: the non-Gd containing intracellular space, the tissue EES, and the blood vessels

which contains Hct and plasma. The CA is assumed to leak across the vascular endothelium and into the EES. This is a passive diffusion and the transfer constant that characterizes the diffuse transport of low-molecular weight Gd across the capillary endothelium is $K^{trans}(\text{min}^{-1})$ [18][22]. K^{trans} can be measured with DCE-MRI and is being used in imaging studies to characterize tumor biology and treatment response. K^{trans} is the constant of proportionality between the concentrations in the blood plasma and the EES and it is related to the flow of plasma into the capillary bed (F_p) and the permeability surface area product (PS) of the endothelial wall [22][14]. $k_{ep}(\text{min}^{-1})$ is a model parameter that accounts for the corresponding rate of Gd from the EES and back to the plasma [14]. The transfer constant k_{ep} is defined as $k_{ep} = K_{trans}/v_e$, where v_e is the volume fraction of the EES [22].

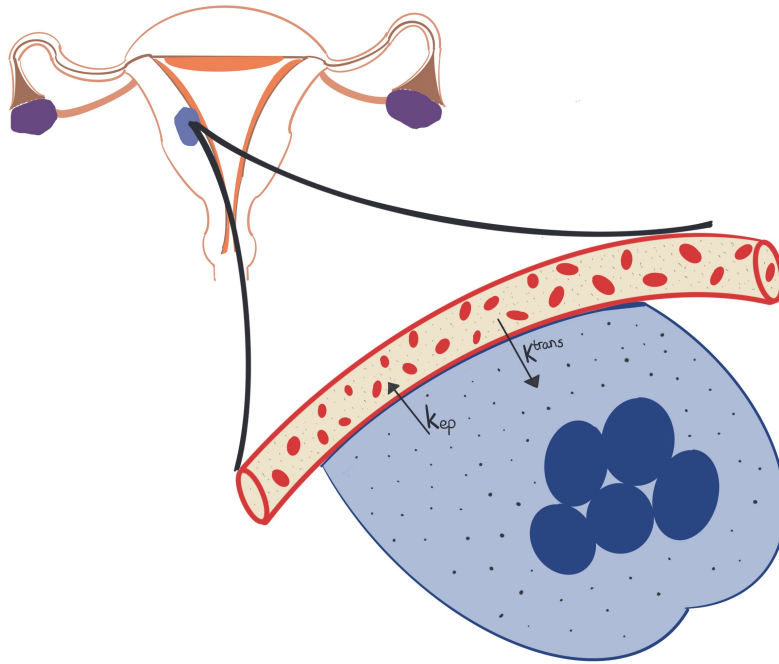


Figure 2.1: An illustration of the parameters in extended Tofts' method. The light blue area is the extravascular extracellular space (EES), while the dark blue space is the intracellular space. The blood vessel contains plasma and red blood cells. The small grey dots in the plasma and in the EES illustrates Gadolinium (Gd). $K^{trans}(\text{min}^{-1})$ and $k_{ep}(\text{min}^{-1})$ are transfer constants, characterizing the transfer of Gd across the endothelium. The relative sizes are not correct in this figure. (illustration inspired by [23]).

ETM, which is found in formula (2.7) gives the concentration-time curve in the tissue of interest, $C_t(t)$. $C_p(t)$ is the concentration-time curve in the plasma of the feeding artery, while $C_e(t)$ is the concentration-time curve in the EES. v_p is the fractional volume of the blood plasma in the tissue of interest [21][22].

$$C_t(t) = C_p(t)v_p + K^{trans} \int_0^t C_p(\tau)e^{-k_{ep}(t-\tau)}d\tau \quad (2.7)$$

Tofts' method (TM) assumes that the fractional volume of the blood plasma, v_p in the tissue is small and makes little contribution to the total concentration of Gd found from the MRI signal. TM is given in equation (2.8), where the first term accounting for the plasma concentration is no longer present in the equation due to the assumption of low concentration of Gd in the plasma [22].

$$C_t(t) = K^{trans} \int_0^t C_p(\tau)e^{-k_{ep}(t-\tau)}d\tau \quad (2.8)$$

ETM given in equation (2.7) includes the contribution from plasma, and is accurate in highly perfused tissues, which means that the blood flow is high [22]. In this case, perfusion means the supply of blood to the tissue and has the unit $ml/min/100ml$ tissue [18]. TM given in equation (2.8) is however accurate in weakly vascularized tissues. A vascularized tissue is a tissue with a capillary network capable of delivering nutrients to the cellular constituents comprising the tissue [22][24].

2.3 Heuristic methods

Heuristic methods are simpler methods for extracting information from DCE-MRI images that might be related to the tissue of interest. Heuristic methods are based on comparing the calculated parameters with observations from previous experiences. These methods include the extraction of parameters that can tell us something about the tissue of interest. Examples of such parameters are peak enhancement (PE), time to peak (TTP), and Area Under Curve (AUC). These derived tissue parameters are independent of imaging sequence parameters such as FA and T_0 if the data acquisition is done correctly. However, if the data acquisition is not done correctly this can influence these parameters. The Heuristic methods have increased variability between both scanners and patients and are dose-dependent. In addition, the calculated parameters may not be clearly related to the characteristics of the biological tissue [18].

PE is the maximum signal intensity of a time-varying signal $S(t)$. TTP is the time before the CA reaches its highest value in the tissue during the first-pass cycle, i.e. before peak enhancement is reached. The concept of PE and TTP is shown in the concentration-time curve in Figure 2.2. AUC is the area under the concentration-time curve, i.e. the area under the curve shown in Figure 2.2. Parameters such as PE, TTP, and AUC might tell us something about a tumor [25].

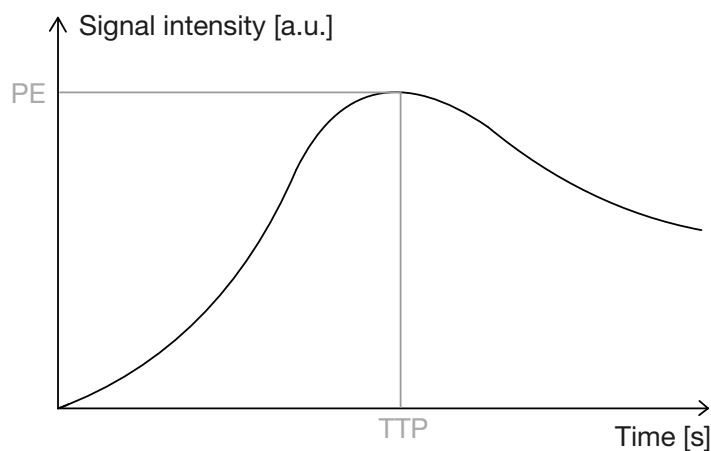


Figure 2.2: An illustration of the parameters peak enhancement (PE) and time-to-peak (TTP), which can be estimated by heuristic methods.

2.4 The Arterial Input function

The AIF is commonly defined as the input concentration of a CA into the tissue of interest. Many of the pharmacokinetic models proposed to analyze DCE-MRI depend on an accurate AIF [15]. Determining the AIF can be difficult due to problems like for instance flow artifacts and partial volume effects [25]. The AIF kinetics is characterized by a sharp uptake, a short-lived peak value followed by a small peak and subsequently, a longer wash-out period, as illustrated in Figure 2.3. This makes the AIF kinetics different from the concentration-time curve in the tissue of interest [25].

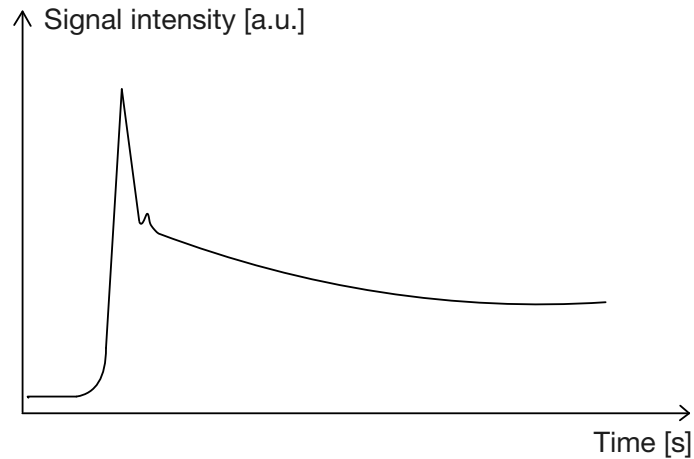


Figure 2.3: The kinetics of the arterial input function (AIF).

There are several ways to estimate the AIF. Three different ways of estimating the AIF will be presented in the next sections.

2.4.1 Manual annotation of the AIF

One way of estimating the AIF is by annotating a region of interest (ROI) on a DCE-MRI image. Ideally, the ROI should be placed in an artery that is feeding the tissue of interest [25]. However, in the case of endometrial cancer, it is not easy to find an artery feeding the uterus from the DCE-MRI images. Therefore, the AIF can be estimated by drawing an ROI in one of the iliac arteries, even though these arteries do not feed the uterus directly [18]. In some cases, it might also be possible to estimate the AIF by drawing an ROI in the aorta [18]. The CA arrives in the aorta and the iliac arteries before it enters the uterus, which can be seen from the DCE-MRI time-series.

2.4.2 Automatic algorithm for detecting the AIF

Another way of estimating the AIF is by implementing an algorithm for segmenting the AIF automatically. Several authors have presented such algorithms, and one of them is Tönnies et al. [26]. The algorithm was proposed based on the properties of the arteries. The concentration of CA in a feeding artery behaves in a specific way giving the signal intensity curve a high peak and a subsequently slower decrease as shown in figure 2.3. The algorithm proposed by Tönnies et al. consists of 9 steps [26].

The algorithm is proposed for DCE-MRI data of colorectal cancer and the principles might be transferred to endometrial cancer data. In summary, the steps of the automatic algorithm for finding the AIF presented by Tönnies et al. are as follows:

1. Select the 1% brightest voxels during a chosen number of time steps. One should choose a number of time steps that cover the arrival time of the CA.
2. Binary opening, which is a morphological operation consisting of an erosion and a dilation step. The goal of this step is to remove small objects, while still keeping the original size and shape.
3. Find the time step with the most peak values and select this time step.
4. Blob and tube filters. The objects that are considered roundish are kept while the rest is discarded.
5. Find the timestep with the most peak values and compare the results to those from step 3.
6. Fit a gamma variate function to the intensity curves. The mask from step 5 is used on all timesteps to find intensity values over time for every voxel. To find objects from the mask, connected component analysis is carried out. The intensity curves for each object are fitted to a gamma variate function and all objects that do not fulfill the selection criteria are discarded.
7. Erosion and dilation.
8. Region growing.
9. Select the two largest objects. The two largest objects are selected because the arteries are present in the left and right half of the volume being imaged.

2.4.3 Population-based AIF

A population-based AIF can be determined by measuring blood samples from a few patients and using the mean concentration from these blood sample measurements as the AIF for all participants [25]. There are also other methods for determining a population-based AIF. For instance, the population-based AIF proposed by Parker et

al [27]. This AIF is synthetic and experimentally derived by looking at data from several patients. The functional form of the Parker AIF was found by fitting a mixture of 2 Gaussians and an exponential modulated with a sigmoid function. The form of the population-based AIF then has a first-pass peak followed by a smaller peak that accounts for re-circulation and then a longer washout period as the signal intensity curve shown in figure 2.3. Several scaling constants can be changed for the Parker AIF to fit the relevant data [27].

2.5 Imaging systems and information flow

The international standard for transmitting, storing, retrieving, printing, processing, and displaying medical images is DICOM (Digital Imaging and Communications in Medicine). DICOM is commonly used for transmitting and storing medical images and can be integrated with devices for medical imaging, such as MRI scanners, workstations, and servers. DICOM files do not only contain medical images but also image-related information. A DICOM object contains many attributes, such as patient ID and image pixel data. Most imaging devices, such as CT, MRI, and Ultrasound have DICOM implemented. DICOM images can be sent to a workstation or a picture archiving and communication system (PACS) [28].

PACS is a system for digital storage, retrieval, display, and transfer of medical images and data. The electronic system was first developed as a diagnostic imaging tool to be used in radiology departments in hospitals. Today, the system can also be used for research purposes through what is called research PACS. In other words, we distinguish between clinical PACS and research PACS. In research PACS the data is anonymized to facilitate research purposes. PACS enables us to electronically transfer diagnostic images like x-rays, CT, MRI, Ultrasound, and PET investigations to other departments and other hospitals [29]. In addition to medical images, PACS can integrate different forms of healthcare data, such as video recordings, text, voice, medical records, and wave images. A PACS consists of different subsystems for image and data acquisition, storage, and display, which are integrated through application software and digital networks [30][31].

Sectra is a vendor that delivers IT solutions for medical purposes, including PACS [32]. The PACS used at MMIV and the Radiology Department at HUS is delivered by Sectra

and is called Sectra clinical PACS and Sectra research PACS. Sectra research PACS is one of the main constituents of the research information system. The main parts of the research information system are Sectra research PACS, Fiona, and REDCap.

REDCap (Research Electronic Data Capture) is a platform for building and managing online databases and surveys in a secure way [33][34]. This web application is especially suitable for capturing data for research studies and operations, both online and offline. Fiona is a web application that allows users to assign, attach, review, and export project data. This is the user interface for uploading new data to the research PACS and transferring data from the clinical PACS to the research PACS, among other things. Fiona is the web application that communicates with both research PACS and REDCap.

The tool for integrating workflows into the research information system is called *ror*. With *ror* you can develop and test a workflow in a simulated research PACS. After testing, a workflow can be built and uploaded to the research PACS. The steps for integrating a workflow into the research information system using *ror* are to create a project directory, configure data and test a workflow on the data. Then build a containerized workflow and test the containerized workflow. The containerized workflow can then be uploaded to the research information system. A project can be integrated into the research information system in order to run the workflow on data in research PACS. A project can then react to the arrival of new data as well. Results from a workflow can be tabulated data or new image data. New image data is added back to the research PACS, while tabulated data is added to REDCap [35].

2.6 Statistical evaluation

For evaluating modeling results it can be convenient to look at the correlation between different results, which is a measurement of whether pairs of variables are related, and how strongly they are related [36]. One way to measure correlation is the Spearman Correlation Coefficient. A Bland-Altman plot can be used for measuring the agreement between quantitative measurement results and statistical tests can be used to measure the statistical significance between results.

Correlation coefficients

The Pearson correlation coefficient is a measurement of the linearity of two measurement results [37]. The linear correlation of two datasets is measured by calculating the ratio between the covariance of two measurements and the product of their standard deviation. The measurements may not be linearly correlated, but can for instance have a relationship that can be described by a monotonic function, which can be measured using Spearman's rank correlation coefficient [37]. The Spearman correlation coefficient is similar to the Pearson correlation coefficient, only calculated with the two variables' ranks instead of their actual values [38]. Ranking the variables makes this test more robust against outliers. Both correlation coefficients have a numerical value ranging from -1.0 to $+1.0$, giving an indication of how strongly the two measurements are related [37][38].

Bland-Altman plot

A Bland-Altman plot can be used to quantify the agreement between two quantitative measurement results. A Bland-Altman plot shows the difference between two measurement results plotted against the mean of these two measurements. Statistical limits are added to the plot based on the mean and the standard deviation of the difference between the two measurements. A confidence interval (CI) of 95% is often used to construct these statistical limits. 95% of the differences in the results from the first and the second method fall within these limits of agreement (LoA). The resulting Bland-Altman plot is a scatter plot of the two measurements A and B, where the y-axis represents $(A - B)$ and the x-axis represents $((A + B)/2)$ [36].

Wilcoxon signed-rank test

The Wilcoxon signed-rank test is a non-parametric test used when comparing two related or matched samples. The test can also be used for repeated measurements of the same sample. The Wilcoxon signed-rank test is the non-parametric equivalent to the parametric paired t-test. While the parametric t-test assumes normally distributed data, non-parametric tests do normally not assume a specific probability distribution. The Wilcoxon signed-rank test gives us a p-value which gives an indication of whether to accept or reject the null hypothesis, which states that the median difference between

the two samples is zero [39][40].

Chi-square test

The chi-square test is a non-parametric test of independence. The test is used to analyze differences between groups by hypothesis testing. The null hypothesis is often used for testing, stating that the categorical data we wish to test has an assumed frequency. The test is used to check whether there is a significant difference between the observed and expected frequencies between two data sets [41][42].

The p-value and statistical significance

A p-value is often listed in quantitative analysis, including in the t-test, the Wilcoxon signed-rank test and the chi-square test. This value gives an indication of whether the obtained research results are statistically significant. The p-value is based on two hypotheses, the null hypothesis and an alternative hypothesis, which often is an assumption of the null hypothesis being not true. The resulting p-value gives us information regarding the probability of our observations with the assumption that the null hypothesis is correct [43][44][45].

Statistical significance measures whether the probability of the null hypothesis is true given a level of uncertainty (α or significance level) regarding the true answer [44]. The significance level is the probability we state that we are willing to be incorrect in our research. If a researcher wants to be correct 95% of the time, then the researcher is willing to be incorrect 5% of the time, which means that the significance level or α is 0.05. A research outcome is statistically significant if the p-value of the analysis is less than α , which is a prespecified value [44].

Receiver Operating Characteristics (ROC)

The receiver operating characteristics (ROC) curve is a plot where the y-axis is defined as the sensitivity or the true positive rate (TPR), while the x-axis is defined as (1 - specificity) or the false positive rate (FPR) [46]. The sensitivity is defined in equation (2.9), where TP is true positives and FN is false negatives. The sensitivity tells us the probability of a test being positive when a disease is present. Equation (2.10) shows

how to calculate the specificity, which tells us whether a test is able to classify if a person is disease-free [47].

$$\textit{Sensitivity} = \frac{TP}{TP + FN} \quad (2.9)$$

$$\textit{Specificity} = \frac{TN}{TN + FP} \quad (2.10)$$

Different cutoff levels for a positive test result are used to generate each point in the ROC curve, which is called an operating point. The area under the ROC curve (AUC ROC) is a popular measure of the overall performance of a diagnostic test. AUC ROC is defined as the average sensitivity value for all positive specificity values. AUC ROC can be between 0 and 1. An AUC ROC close to 1 shows a good diagnostic performance of the test. A test that has an AUC ROC value of 1 is perfectly accurate [46].

Chapter 3

Materials and methods

This chapter includes patient materials, the imaging protocol used for acquiring the DCE-MRI images and information on how the tumor masks were segmented. The chapter also includes the procedure used for estimating the AIF using three different methods and the procedure for modeling with ETM. Two different environments were utilized for modeling, a local modeling environment allowed for testing of different AIFs, in addition to erosion and dilation of tumor masks. The environment of the research information system allowed for the processing of more patient data. The procedure for integrating a workflow into the research information system is included in this chapter, as well as how the model parameters derived from ETM were evaluated.

3.1 Patient data

The patients included in this project underwent preoperative pelvic DCE-MRI from 2009 to 2014 and were randomly selected from a larger patient cohort. In total, 64 patients were included in the project. Data from 63 of these patients were analyzed in the research environment. Data from 19 of the patients analyzed in the research environment, were also analyzed in a local modeling environment, whereas data from one patient were only analyzed in the local modeling environment. The patients included in this project were diagnosed with low-risk or high-risk endometrial cancer, where low-risk cancers were endometrioid of grade 1 or 2, whereas high-risk cancers were non-endometrioid or endometrioid of grade 3.

3.2 Imaging protocol

Imaging was performed on a 1.5-T MRI scanner (Siemens Avanto running Syngo v. B17, Erlangen, Germany) using a six-channel body coil and a standardized imaging protocol [1][48][11]. 20 mg butyl-scopolamine bromide (Buscopan; Boehringer, Ingelheim, Germany) was administered intravenously before scanning to reduce motion artefacts. Structural MRI images include pelvic sagittal and axial oblique (perpendicular to the long axis of the uterus) T2W images, together with axial oblique T1W gradient-echo images before and 2 min after intravenous administration of CA (Dotarem, Guerbet (Paris, France): 0.1 mmol Gadolinium per kilogram of body weight, 3 mL/s injection speed). Physiological MRI images include Pelvic DCE-MRI obtained for 12 oblique axial slices applying a 3D spoiled gradient echo (FLASH) sequence where $TE/TR = 1.05/2.64ms$, flip angle $[FA] = 12^\circ$, matrix = 256x256, field of view (FOV) = 300x300mm², slice thickness = 5mm, number of averages $[NA] = 1$) with a temporal resolution of 2.49s. Sequential images were acquired from 30s before intravenous administration of CA to 6.3min after CA injection. At 2 min post-CA administration, a pause of 33s was utilized to acquire the diagnostic T1W contrast-enhanced series [12]. All images being analyzed in this project were acquired at HUS.

3.3 Tumor segmentations

The primary tumor masks used in this project were segmented by two experienced radiologists at HUS. The manual segmentations were performed on whole-volume data, more specifically on the VIBE (volumetric interpolated breath-hold examination) images. A value of 1 was assigned to the primary tumor tissue, while a value of 0 was assigned to the remaining tissue. The two radiologists were both blinded to the segmentations of each other.

3.4 The arterial input function

Three different methods for estimating the AIF were implemented in Python [49]. Version 3.10.9 of Python was used throughout the present project and the scripts are available in Appendix 6. A visual approach was used to evaluate if an estimated AIF was

accurate or not. An AIF curve with a high and narrow first peak and a longer washout period with relatively little noise was assumed to be a good AIF. Such an AIF is illustrated in figure 2.3 in section 2.4.

3.4.1 Manual annotation of the AIF

AIFs were manually annotated on DCE-MRI data from 20 patients using the Image-data library in Python [49][50]. Version 2.0.0 of Imagedata was used in this project. The annotations were performed by subtracting the baseline signal from the DCE-MRI images and subsequently drawing an ROI on a slice where the CA was first seen entering the iliac arteries or the aorta. The majority of the AIF masks were annotated in the iliac arteries (n=18), but for a few patients (n=2), the aorta was available in the image. The baseline signal was approximated by calculating the mean MRI signal from the first 5 time points. The final AIF was estimated by calculating the mean signal intensity inside the annotated ROI. The manual annotations were only performed on one slice. The iliac arteries and/or the aorta are oriented differently in the DCE-MRI images. Therefore, the AIF ROIs were placed in different areas of the DCE-MRI images depending on where the aorta or the iliac arteries were located. Due to the varying anatomy between the patients, the coordinate system of the MRI machine is changed during imaging according to the orientation of the uterus. Certain annotated AIF ROIs were comprised of a larger number of voxels than others because the desired arteries were of different sizes in the DCE-MRI images.

3.4.2 Semi-automatic algorithm for detecting the AIF

A semi-automatic algorithm for detecting the AIF was implemented in Python. The algorithm is based on the one proposed by Tønnes et al., which was briefly explained in section 2.4.2 [26]. An in-house implementation of the AIF algorithm¹ fitted to kidney data was revised to fit endometrial cancer data. The resulting algorithm was semi-automatic and not automatic because different percentages of bright voxels were tested in the first step of the algorithm. 20 time steps seemed sufficient for covering the arrival time of the CA. This assumption was based on analyzing the DCE-MRI images visually when the annotations of the AIFs were performed. The arterial size of the desired

¹The automatic AIF algorithm was implemented by Erling Andersen

artery may differ between what organ is investigated, hence different percentages of bright voxels were tested. A portion of bright voxels of 1%, 2%, and 3% were tested for DCE-MRI data from 20 patients. The discard criteria was based on a cost value after optimization of a gamma variate function. Optimization was performed using the SciPy library of version 1.9.3 in Python and solving a nonlinear least-squares problem [49][51].

3.4.3 Population-based AIF

A population-based AIF was calculated based on manually annotated AIFs from 20 patients. The population-based AIF was calculated as the mean AIF from the manually annotated AIFs. It was assumed that the peak of the AIF curve arise at the same time for all patients. The CA is injected at approximately the same time for all patients, but due to differences in cardiovascular function between the patients, the CA will not arrive in the tissue of interest at the exact same time for all patients.

3.5 Extended Tofts' method

ETM was implemented in Python [49]. Two different environments were used for modeling. In a local modeling environment, the three different AIFs were tested on data from 20 patients diagnosed with endometrial cancer. The three different AIFs tested in the local modeling environment include manual annotation of the AIFs, a population-based AIF and a semi-automatic algorithm for estimating the AIF. In addition, ETM was implemented in the research information system where the model was tested on data from 63 patients diagnosed with endometrial cancer. These two environments were handled separately from each other, even though data from some patients were analyzed in both modeling environments.

3.5.1 Analytical solution

ETM was solved analytically. The differential equation shown in equation (2.6) in section 2.2 was solved using an integrating factor. The resulting equation is ETM given in equation (2.7) in section 2.2.1. The mathematical derivation of ETM can be found

in Appendix A.1.

3.5.2 Python implementation

ETM was implemented in Python for numerical modeling [49]. The implemented algorithms used for modeling are available in Appendix 6. All of the images that were analyzed in this project were DICOM images. Two images were required for modeling, the whole-volume tumor masks and the DCE-MRI images.

Before further processing, the baseline signal was subtracted from all of the voxels in the DCE-MRI data. The baseline signal is the MRI signal before the CA is injected into the patient. The baseline signal was calculated as the mean signal intensity from the first 5 time points. Enhancement from CA appears around 45-50 seconds into the DCE-MRI recording, which is approximately time point number 20 since the temporal resolution of the DCE-MRI images was 2.49 seconds. After subtracting the baseline signal, the remaining signal intensity was used as the raw tissue concentration in ETM, as suggested by Hanson et al. [52]. Therefore, the signal intensity will be the employed expression moving forward, and not the tissue concentration.

The whole-volume tumor mask was aligned with the DCE-MRI image. The tumor mask was annotated on a structural MRI image and the dimensions of the images differ. Consequently, a co-registration was performed to change the dimension of the tumor mask. Co-registration was performed using an in-house function² revised for the purpose of the current study. By utilizing this function, the grid of the whole-volume tumor mask was changed to fit the grid of the dynamic image.

After aligning the structural image and the dynamic image by a co-registration, the average signal intensity from the voxels inside the tumor was calculated. Subsequently, ETM was fitted to the average signal intensity inside the tumor mask. Equation (2.7) in section 2.2.1 was implemented in Python and the parameters K^{trans} , v_e , and v_p were optimized using non-linear least squares to fit ETM to the signal intensity inside the tumor. The SciPy Python library was used to derive model parameters from ETM [49][51]. ETM was first fitted to the average signal intensity inside the tumor mask. Secondly, the model was fitted to the signal intensity from each voxel inside the tumor. After optimizing perfusion parameters from each voxel K^{trans} , v_e , and v_p were

²Function for image alignment implemented by Erling Andersen and Erlend Hodneland

established by calculating the mean from the optimized parameters from each voxel. The transfer constant k_{ep} was calculated from K^{trans} and v_e , by utilizing the coherence $k_{ep} = K^{trans}/v_e$ [22].

The input plasma concentration C_p was calculated from the AIF by using the formula given in equation (2.4) in section 2.2. It was assumed that all patients had a Hct of 42% [21]. The portion of Hct will differ slightly between patients, but the amount of Hct was not measured for each individual patient.

The tumor volume was also calculated. The tumor volume was calculated by multiplying the size of the voxels with the number of voxels making up the tumor mask. The tumor volume was then multiplied by 0.001 to convert from mm^3 to ml.

Local modeling environment

For modeling locally, ETM was tested on data from 20 patients. The DCE-MRI images and the whole-volume tumor masks used for modeling locally were downloaded from Sectra research PACS. This modeling environment utilized testing of different modeling configurations, like the AIF methods and erosion and dilation of tumor masks. Three different methods for estimating the AIF were tested on all 20 patients.

For modeling locally and using the population-based AIF, erosion and dilation of the tumor masks were tested. An erosion was performed to make the tumor masks smaller, while a dilation was performed to make the tumor masks larger. Erosion and dilation were performed to establish whether the parameters derived from ETM change when the size of the tumor masks is changed. The co-registration between the tumor masks and the DCE-MRI images may lead to registration artefacts. By increasing and decreasing the size of the tumor masks we might get an indication of whether normal myometrium is present in the tumor masks or not after image alignment. If normal myometrium is present in the tumor masks the optimized parameters are expected to change slightly because of differences in the biology of normal myometrium and endometrial cancer tissue.

Parameter maps were created for all K^{trans} , k_{ep} , v_e , and v_p values inside the tumor for one patient. These maps show the values of the parameters for each voxel of tissue. This was only conducted for the manual AIF method as an illustration of the calculated parameters. The parameter maps illustrate that the values of the calculated perfusion

parameters vary inside the tumor. All of the voxels outside the tumor were assigned to be zero.

Research modeling environment

The second environment where ETM was implemented is the research information system at MMIV and the Radiology Department at HUS. Data from 63 patients were analyzed in the research information system. For this purpose, the population-based AIF was used. In the following section, it is explained how a workflow for running ETM was implemented into the research environment.

3.6 Integration into the research information system

A workflow for optimizing perfusion parameters using ETM was integrated into the research information system at MMIV. The goal with this was to integrate a workflow in order to run ETM on data from a larger number of patients which is found in Sectra research PACS. The `ror` tool was used for this purpose and the results were tabulated and added to REDCap [35]. In order to integrate the workflow into the research information system, a docker container was made of the project, which was uploaded to the research information system. The docker container was uploaded to Fiona, where DCE-MRI data and tumor masks were extracted from Sectra research PACS. ETM was then used to derive perfusion parameters from the data. The derived parameters and the tumor volumes were tabulated and added to REDCap.

A population-based AIF was used for modeling in the research information system. A lot of testing was done locally before the workflow could be uploaded to Fiona. For selecting the right patient data, a select statement was formulated with a syntax similar to SQL. The chosen select statement was *'select participant from study where series named "MASK" has SeriesDescription regexp "(JAD|KWL)" also where series named "DCE" has NumImages > 1500 and SeriesDescription regexp "12"*. JAD|KWL means to select images that contain the regular expression JAD or KWL. This expression was included to select the tumor masks because only the whole-volume tumor masks have this expression added to their *SeriesDescription*. *SeriesDescription* and *NumImages* are attributes to the DICOM objects.

Most DCE-MRI images being analyzed in this project have 1920 images because there are 12 slices and 160 time points for each slice. Since the DCE-MRI data have a large number of images, only dynamic sequences with over 1500 images would pass the select statement. In the *SeriesDescription* for the DCE-MRI sequence the number 12 is often included because the FA is 12°. The *SeriesDescription* is usually formulated as "Dynamic Flip 12" or something similar, but since the *SeriesDescription* is written by humans the *SeriesDescription* will differ between patients. In order to see if more patient data could be processed, the *SeriesDescription* for the DCE-MRI images were removed from the select statement. That means that the select statement *'select participant from study where series named "MASK" has SeriesDescription regexp "(JAD|KWL)" also where series named "DCE" has NumImages > 1500'* was also tested.

3.7 Evaluation

Different methods were utilized for analyzing the model parameters from ETM. Methods for quantifying the agreement between the resulting parameters were necessary as both different methods for modeling and different methods for estimating the AIF were tested. Methods for establishing whether there is a correlation between the derived perfusion parameters and histologic tumor grade were also implemented.

3.7.1 Evaluating results from the local environment

Comparing average and voxelwise model parameters

The difference between the model parameters from average and voxelwise modeling was analyzed for all AIF methods. The mean K^{trans} , k_{ep} , v_e and v_p parameters were tabulated in addition to the standard deviations. The mean absolute differences between the model parameters derived from the average and voxelwise modeling methods were also tabulated, in addition to the percent wise differences. The derived K^{trans} values were analyzed in more detail. The absolute differences between the K^{trans} values from average and voxelwise modeling were plotted against the tumor volume. The absolute differences between the derived k_{ep} values were also plotted against the tumor volume.

Comparing model parameters from ETM using different AIF methods

For comparing the model parameters from ETM when using different methods for estimating the AIF, only the parameters obtained from modeling based on the average signal intensity were analyzed. The mean absolute differences between the derived K^{trans} , k_{ep} , v_e and v_p values were tabulated. The percent wise differences were also calculated and added to the table. The median model parameters were also tabulated for all AIF methods, in addition to the range of the parameters. The signal intensity curves from ETM were plotted together with the AIF curves and the tissue signal intensity curves before modeling. Signal intensity curves were visualized for the three AIF methods. The curves were based on data from two different patients. The same patient data was visualized for all AIF methods for comparison.

3.7.2 Evaluating results from the research environment

The parameters derived from the research information system when using a population-based AIF were also analyzed. The mean model parameters derived from average and voxelwise modeling were tabulated, in addition to the standard deviations and the absolute difference between the results from average and voxelwise modeling. In addition, the median of the derived parameters was tabulated together with the range of the parameters.

The results obtained from the research information system were also analyzed for correlations with histologic tumor grade. The endometrioid histologic type of grade 3 and the non-endometrioid histologic type constitutes the high-risk histologic tumor grades. The low-risk tumor grade is comprised of the endometrioid histologic type of grades 1 and 2. Data from 60 out of 63 patients were analyzed for correlations with histologic grade because the histologic grades were missing for 3 patients (n=60). The median K^{trans} , k_{ep} , v_e and v_p values were calculated for the low-risk histologic grade and the high-risk histologic grade and tabulated together with the range of the values.

3.7.3 Statistical considerations

For all statistical analyses, a significance level of 5% was chosen ($\alpha = 0.05$).

A function for plotting a Bland-Altman plot was implemented in Python. Bland-Altman plots were used for analyzing the agreement between model parameters derived from the average and voxelwise modeling methods. The method was also used to quantify the agreement between the model parameters from ETM using different methods for estimating the AIF.

It was decided to use Spearman's correlation coefficient because the derived parameters were not normally distributed. The SciPy library in Python was used for this purpose [49][51]. Firstly, the method was used to measure the correlation between the model parameters from ETM when modeling based in the average signal intensity and modeling based on the voxelwise signal intensity. Secondly, the method was used to measure the correlation between the parameters derived from ETM when three different AIF methodologies were used.

The Wilcoxon signed-rank test was used for comparing the derived K^{trans} values from ETM using the average and the voxelwise modeling methods. In addition, the test was used for comparing the K^{trans} parameters derived from ETM when using different methods for estimating the AIF. The SciPy library in Python was used for this purpose [49][51]. The Wilcoxon signed-rank test was chosen over the student's t-test because the results were paired, but not normally distributed.

A chi-square test was performed to test whether the observed K^{trans} values were as expected in terms of low-risk and high-risk histologic grade. The K^{trans} values were split on the median value, dividing the K^{trans} values into two groups, $K^{trans} > K_{median}^{trans}$ and $K^{trans} < K_{median}^{trans}$. These two groups were then chosen as expected low-risk and high-risk histologic tumor grades in the chi-square test. The observed frequencies of low-risk and high-risk histologic tumor grade were then tested using the SciPy library in Python [49][51].

ROC curves were created in Python using the scikit-learn library [49][53]. The ROC curves were created to check whether there is a correlation between the derived perfusion parameters and histologic tumor grade. ROC AUC values were also calculated using the same Python library and added to the ROC plots.

Chapter 4

Results

The results are presented in this chapter. Firstly, we present the resulting AIFs from three different methodologies, including manual annotation of the AIF, a semi-automatic algorithm for estimating the AIF and a population-based AIF. Secondly, we present the model parameters from ETM using the three AIF methods. The resulting model parameters from modeling in the research information system are also included in this chapter, as well as a correlation analysis between the derived model parameters and histologic tumor grade. Both the mean and average values presented in this chapter are arithmetic mean values.

4.1 The arterial input function

4.1.1 Manually annotated AIF

Manual AIFs were annotated on DCE-MRI data from 20 patients ($n=20$). Variations in the difficulty of manually estimating the AIFs were experienced when the segmentations were executed. The variations in the difficulty of annotating AIF ROIs are illustrated in Figure 4.1, where it is shown that the right AIF curve consists of more noise and has a lower peak value than the left AIF curve. In addition, the right AIF ROI is smaller and consists of fewer bright voxels than the left AIF ROI. The dicom attribute *sliceLocations* shows that the locations of the slices differ between the DCE-MRI images from the two patients shown in Figure 4.1. As a consequence, the DCE-MRI images look different for the two patients. The arteries are sliced and imaged in different ways depending on the anatomy of the patient. The peak value of the left AIF curve

is very high, which might be because the AIF ROI was annotated in the aorta and not in one of the iliac arteries. Two minutes post CA injection we observed a break in imaging. This is illustrated from the AIF curves in Figure 4.1, between 100 and 200 seconds into the dynamic imaging sequence. In this imaging break, a different MRI sequence is acquired.

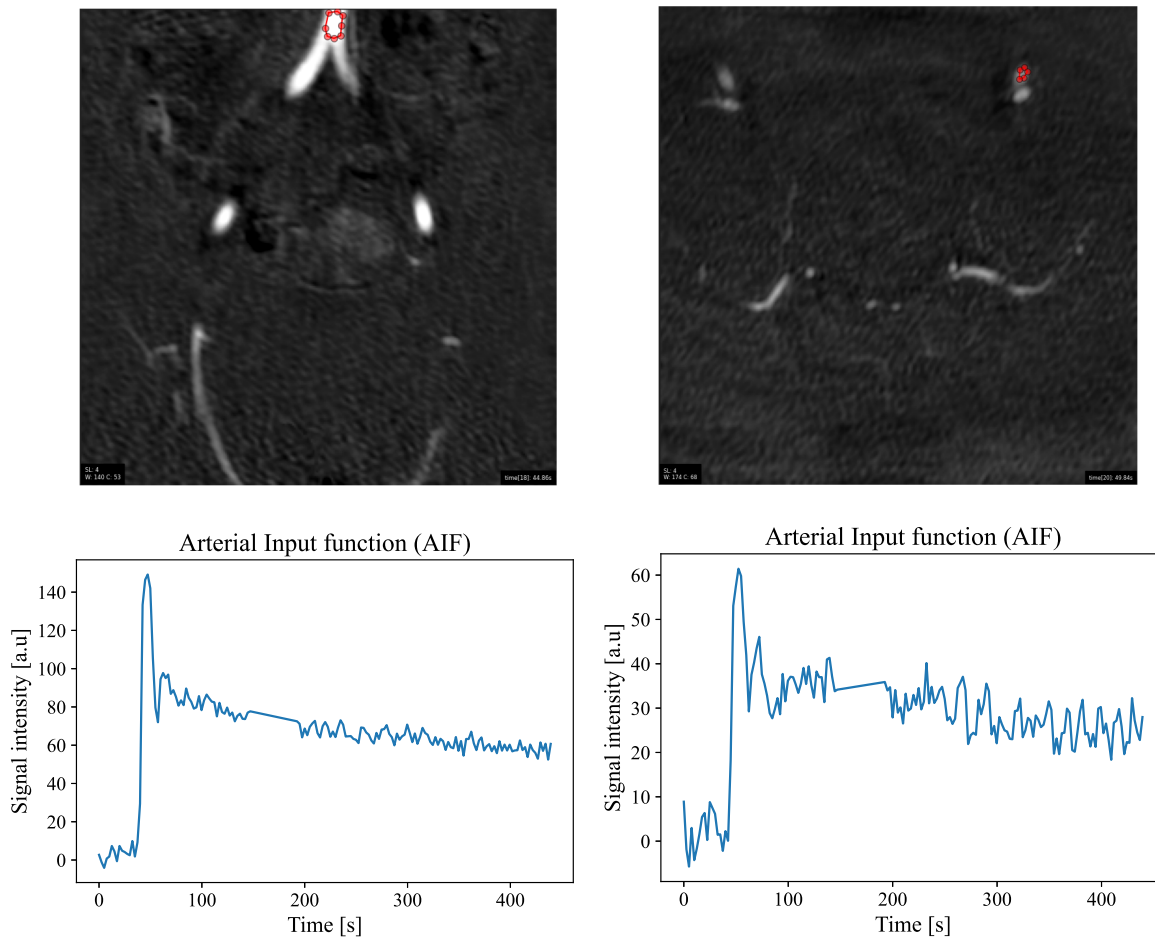


Figure 4.1: DCE-MRI images from two different patients showing the placement of regions of interest of the arterial input function (AIF) and the corresponding AIF curves. The left AIF curve corresponds to the left image, while the right AIF curve corresponds to the right image. More noise and a lower peak value are illustrated in the right AIF curve.

4.1.2 Semi-automatic AIF algorithm

The semi-automatic algorithm was able to find an AIF with a shape similar to the one proposed in Figure 2.3 in section 2.4 for the patients that had an artery where several voxels were visible in the DCE-MRI images. For instance, the algorithm managed to find an AIF with the right shape for the patient shown to the left in Figure 4.1. Contrary, the AIF curve estimated for the patient shown to the right in Figure 4.1 was very noisy

and did not have a distinct peak value. This is illustrated in Figure 4.2, which shows AIF curves derived from the same patient data as the curves illustrated in Figure 4.1, only by the semi-automatic AIF method. From Figure 4.2 it is shown that the left AIF curve looks similar to the AIF curve in Figure 2.3, where the first peak is high and narrow with a subsequent longer washout period. In contrast, the right curve in Figure 4.2 does not have a clear peak value and is noisy, here the algorithm seems to have failed in estimating an AIF.

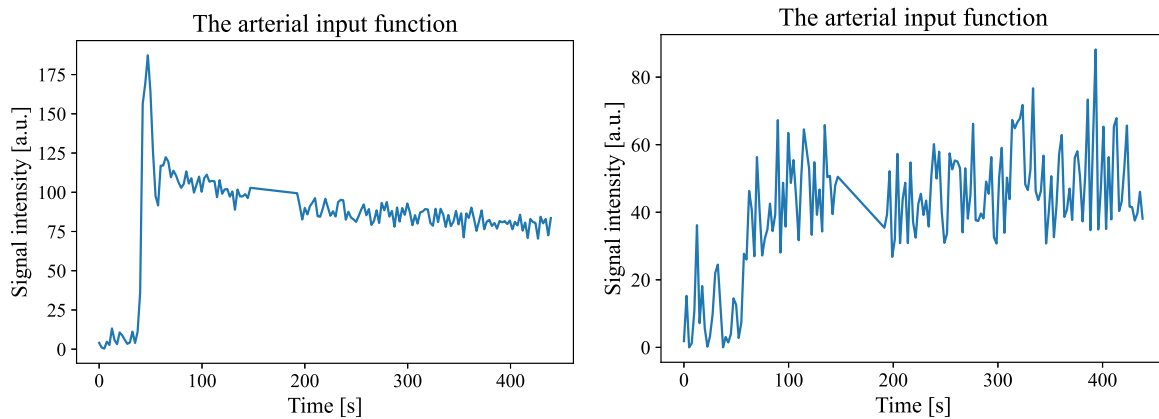


Figure 4.2: Arterial input function (AIF) curves estimated from the semi-automatic AIF algorithm. The left AIF curve is based on the same patient data as the manually segmented AIF curve illustrated to the left in figure 4.1. The right AIF curve is based on the same patient data as the manually segmented AIF curve illustrated to the right in figure 4.1. The left curve looks like the desired AIF curve, while the right curve seems to be noise with no distinct peak value.

Different percentages of bright voxels in the first step of the algorithm resulted in different AIF results. For a portion of bright voxels of 1%, the semi-automatic algorithm only managed to find an AIF for 3 out of 20 patients. The results from these three patients were not analyzed due to a poor basis for comparison. For a portion of bright voxels of 2%, the algorithm managed to find an AIF for 13 out of 20 patients. The algorithm managed to find an AIF with the shape illustrated in Figure 2.3 in section 2.4 for 7 of these patients. This evaluation is based on the visual shape of the resulting AIFs. In terms of the shape of the resulting AIFs, the algorithm works for approximately 35% of the cases for 2% bright voxels. For a portion of bright voxels of 3%, the algorithm found an AIF for 18 out of 20 patients, but only one of the 18 patients had an AIF curve with a high and narrow first peak and a longer washout period.

The slice locations of the DCE-MRI time-series data differ between the patients making the arteries differ in size and shape in the DCE-MRI images. It looks like the algorithm struggled to find AIFs with the shape as illustrated in Figure 2.3 for DCE-MRI data

where the slices were located in a way that make the iliac arteries small. This evaluation is based on visual examinations of the DCE-MRI data. The orientation of the DCE-MRI images seems to affect the performance of the semi-automatic AIF algorithm. Cost values for 2% and 3% brightest voxels are listed in Appendix B.1. These cost values substantiate how well a calculated AIF curve fits a Parker population AIF.

4.1.3 Population-based AIF

Figure 4.3 shows a plot of the calculated population-based AIF. The AIF curve has a high and relatively narrow first peak and a longer washout period. The small peak accounting for re-circulation is also shown right after the first high peak in the curve. Little noise is observed in the population-based AIF illustrated in Figure 4.3.

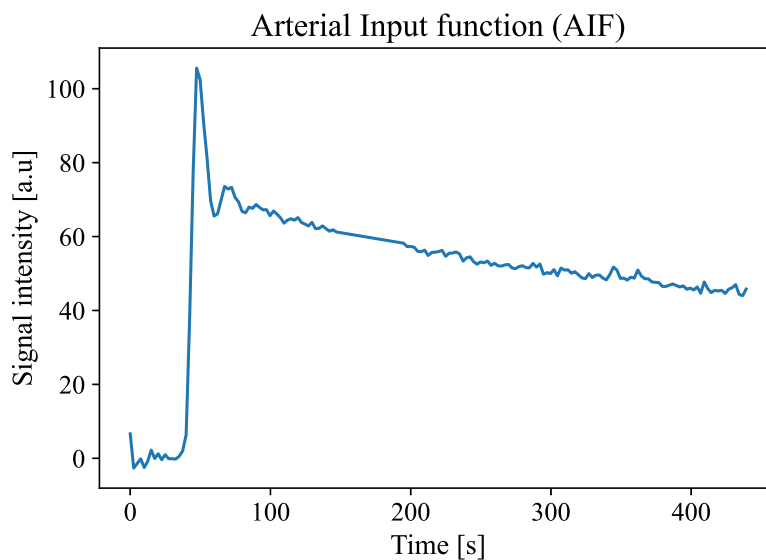


Figure 4.3: The population-based arterial input function, which was calculated based on manually annotated AIF data from 20 patients.

4.2 Extended Tofts' method

Results from ETM were obtained from two different modeling environments. In the local modeling environment three different methods for estimating the AIF were tested (n=20). In the research information system, the population-based AIF method was utilized to estimate perfusion parameters from a larger number of patients (n=63). All model parameters derived from ETM can be found in Appendix A.2.

4.2.1 Local modeling environment

Comparing average and voxelwise modeling results

Table 4.1 shows the mean model parameters from ETM when using different methodologies for estimating the AIF. The results from all AIF methods were based on the same patient data. The table summarizes the differences between the parameters derived from modeling based on the average signal intensity inside the tumor and modeling based the voxelwise signal intensity inside the tumor. The biggest absolute mean K^{trans} difference is observed for the population-based AIF method. However, the differences in K^{trans} and v_p are small for all AIF methods. The largest absolute mean differences between the parameters derived from the average modeling method and the voxelwise modeling method are observed for k_{ep} , and the mean absolute differences are the largest for the semi-automatic AIF methods.

Table 4.1: Mean model parameters and standard deviations from extended Tofts' method when using different methods for estimating the arterial input function (AIF). v_e and v_p are fractions of the total tissue volume inside a voxel, K^{trans} and k_{ep} have the unit min^{-1} . The absolute mean difference is also included. Higher mean values and absolute mean differences are observed for the semi-automatic AIF methods. 2% and 3% are the portions of bright voxels for the semi-automatic AIF.

Manual AIF (n=20)	K^{trans}	k_{ep}	v_e	v_p
Average	0.16 ±0.09	0.78 ±0.59	0.30 ±0.20	0.18 ±0.07
Voxelwise	0.16 ±0.08	0.76 ±0.44	0.33 ±0.17	0.18 ±0.08
Difference	0.0003 (0.18%)	0.02 (2.9%)	0.03 (9.1%)	0.0004 (0.22%)
Population-based AIF (n=20)	K^{trans}	k_{ep}	v_e	v_p
Average	0.12 ±0.05	0.65 ±0.50	0.27 ±0.19	0.19 ±0.08
Voxelwise	0.13 ±0.05	0.84 ±0.50	0.31 ±0.15	0.19 ±0.08
Difference	0.011 (8.7%)	0.19 (25.8%)	0.036 (12.4%)	0.001 (0.53%)
Semi-automatic AIF (2%, n=13)	K^{trans}	k_{ep}	v_e	v_p
Average	0.52 ±0.80	1.19 ±1.56	0.35 ±0.34	0.37 ±0.18
Voxelwise	0.53 ±0.78	3.07 ±4.47	0.40 ±0.26	0.37 ±0.18
Difference	0.004 (0.68 %)	1.87 (88.0%)	0.052 (13.9%)	0.002 (0.60 %)
Semi-automatic AIF (3%, n=13)	K^{trans}	k_{ep}	v_e	v_p
Average	0.29 ±0.44	0.58 ±0.66	0.51 ±0.39	0.36 ±0.17
Voxelwise	0.29 ±0.42	9.29 ±22.9	0.54 ±0.26	0.37 ±0.14
Difference	0.001 (0.40%)	8.72 (177%)	0.03 (5.4%)	0.016 (4.5%)

Figure 4.4 shows plots of the absolute differences in K^{trans} from modeling based on the average signal intensity and from modeling based on the voxelwise signal intensity. The K^{trans} differences were plotted against the tumor volumes to see if there is any coherence between the differences in K^{trans} and the tumor volumes. From Figure 4.4 we observe larger differences in the K^{trans} values when using the semi-automatic AIFs. It does not seem to be a clear coherence between the K^{trans} differences from average and voxelwise modeling and the tumor volumes.

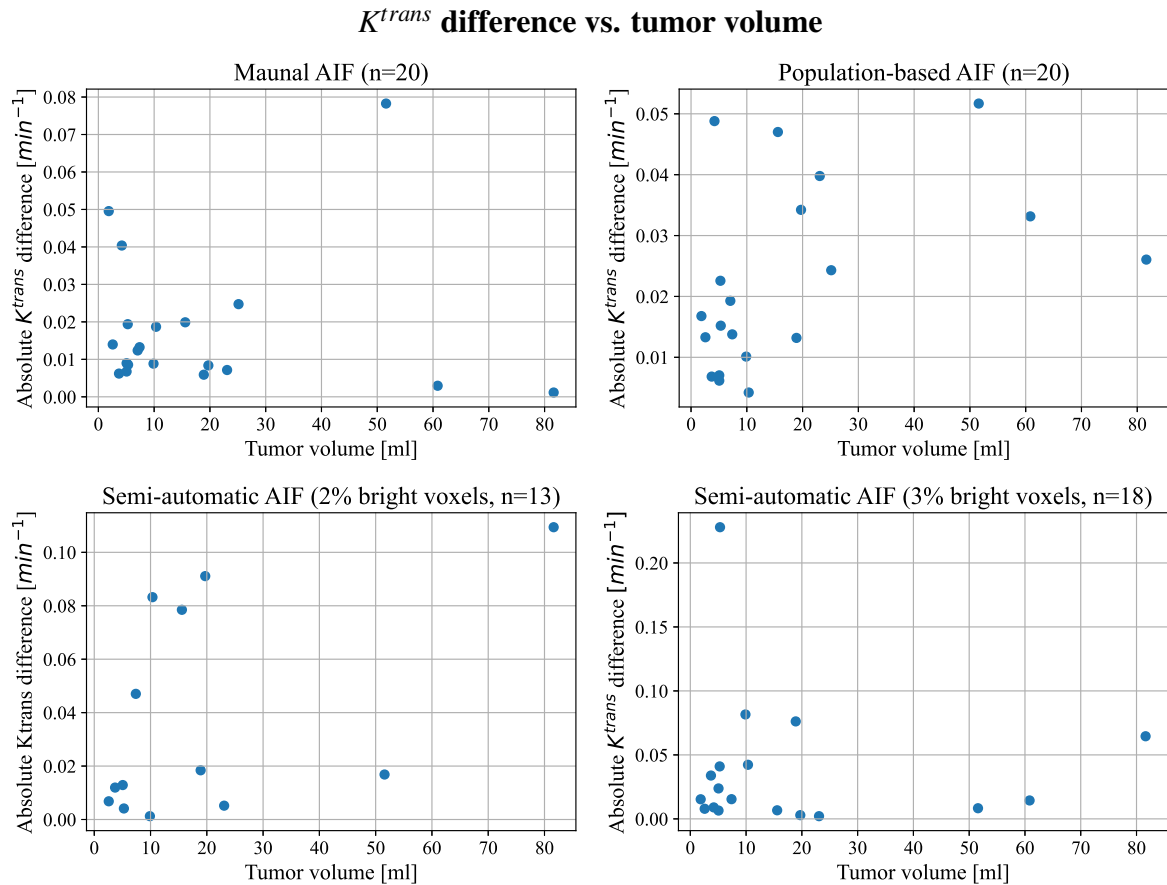


Figure 4.4: The absolute differences in K^{trans} derived from extended Tofts' method when modeling based on the average signal intensity and from modeling based on the voxelwise signal intensity inside a tumor. Four different methods were used for estimating the arterial input function (AIF). The y-axis of the different plots are of different ranges, illustrating differences between the derived K^{trans} values when using different AIF methods.

Figure 4.5 shows Bland-Altman plots of the derived K^{trans} values when modeling based on the average signal intensity and modeling based on the voxelwise signal intensity inside the tumor. The biases are $-0.0003min^{-1}$ (0.18%), $-0.0111min^{-1}$ (8.68%), $-0.0035min^{-1}$ (0.68%) and $-0.0012min^{-1}$ (0.40%) for the manual AIF method, the population-based AIF method, the semi-automatic AIF method when choosing 2% bright voxels and the semi-automatic AIF method when choosing 3% bright voxels,

respectively. This indicates that the voxelwise method on average measures slightly higher K^{trans} values for all AIF methodologies, even though the difference is small. From Figure 4.5 it is shown that the axes have a higher range and that the LoAs are higher for the semi-automatic AIF methods. Most of the points in the plots have low mean K^{trans} values and low differences between the derived values. However, the semi-automatic AIF methods seem to result in more outliers in the K^{trans} values derived from ETM.

K^{trans} Bland-Altman plots

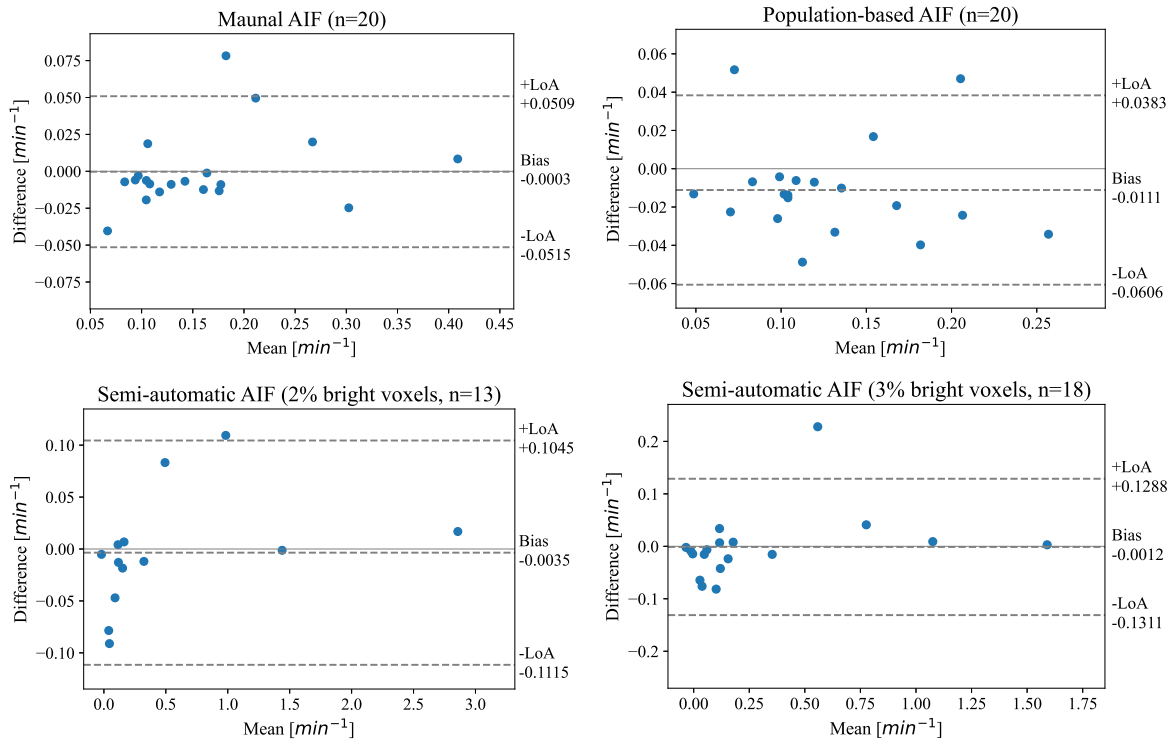


Figure 4.5: Bland-Altman plots of the derived K^{trans} values from extended Tofts' method using four different methods for finding the arterial input function (AIF). The difference between the derived K^{trans} values from average and voxelwise modeling are here analyzed. +LoA and -LoA show the upper and lower limits of agreement, respectively. The y-axis range differs between the plots. Small bias is observed for all AIF methods.

The derived K^{trans} parameters from modeling based on the average signal intensity and from modeling based on the voxelwise signal intensity are positively correlated for all four AIF methods and the correlation is statistically significant (p-values < 0.05). All of the calculated Spearman correlation coefficients and p-values can be found in Appendix A.3.1.

The Wilcoxon signed-rank test gives evidence to accept that the median is different between the K^{trans} values derived from modeling based on the average and the voxel-

wise signal intensity for the population-based AIF method (p-value < 0.05). Contrary, the Wilcoxon signed-rank test gives evidence to accept that the median K^{trans} derived from two other AIF methodologies when modeling based on the average and the voxelwise signal intensity are similar (p-values > 0.05). The calculated p-values from the Wilcoxon signed-rank test can be found in Appendix A.3.2.

Figure 4.6 shows the absolute differences between the derived k_{ep} values from ETM when modeling based on the average signal intensity inside the tumor and from modeling based on the voxelwise signal intensity inside the tumor and calculating the average afterward. From Figure 4.6 we observe a few large outliers in the derived k_{ep} values from the semi-automatic AIF methods. The absolute differences are largely due to large k_{ep} values derived from the voxelwise modeling method. The outliers occur at low tumor volumes.

k_{ep} difference vs. tumor volume

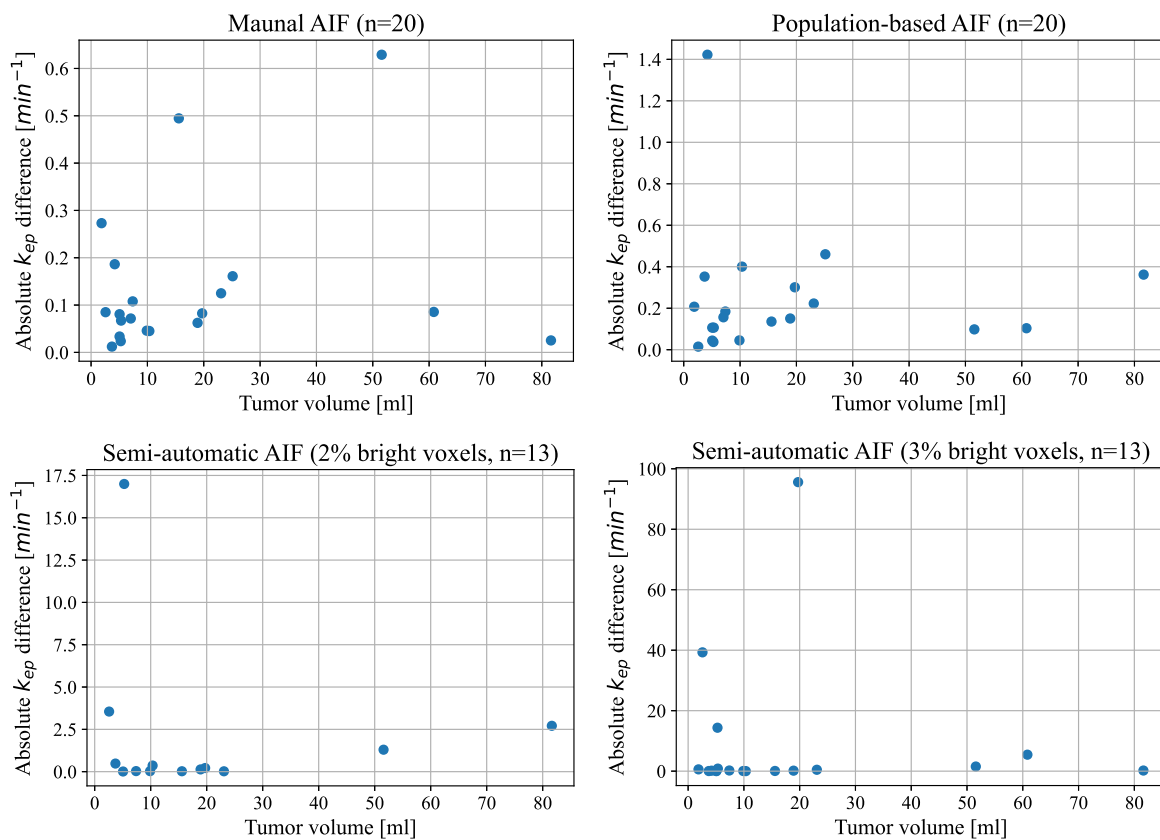


Figure 4.6: The absolute differences between the derived k_{ep} values from extended Tofts' model when modeling based on the average signal intensity and modeling based on the voxelwise signal intensity inside the tumor. The values are plotted against the tumor volume. The y-axis range differs in the four plots.

Comparing the results from ETM when using different AIF methods

For comparing different AIF methodologies, only the model parameters derived from the semi-automatic algorithm when 3% bright voxels were chosen in the first step of the algorithm, was used as a basis for comparison. From now on, the semi-automatic AIF algorithm means the semi-automatic algorithm with 3% bright voxels. Table 4.2 shows summaries of the absolute mean differences between the parameters derived from ETM. Table 4.2 shows that the absolute mean differences are larger when comparing the parameters derived from the semi-automatic AIF method with the parameters derived from the two other AIF methodologies.

Table 4.2: A summary of the absolute mean differences in the parameters derived from extended Tofts' method when different methods for estimating the arterial input function were used. K^{trans} and k_{ep} have the unit min^{-1} , while v_e and v_p are fractions of total tissue volume inside a voxel. The percent wise differences are included in parentheses.

	Population-based vs. manual AIF (n=20)	Manual vs. semi-automatic AIF (n=18)	Population-based vs. semi-automatic AIF (n=18)
K^{trans}	0.053 (37.4%)	0.29 (120.1%)	0.27 (130.3%)
k_{ep}	0.23 (38.8%)	0.20 (110.1%)	0.73 (128.0%)
v_e	0.061 (24.1%)	0.31 (82.9%)	0.33 (89.9%)
v_p	0.044 (22.9%)	0.22 (86.2%)	0.21 (83.5%)

Table 4.3 shows median values derived from ETM when different AIF methodologies were used. The median K^{trans} values are more similar between the AIF methods than the mean K^{trans} values. However, the range of the derived model parameters is higher for the semi-automatic AIF method than what is observed for the two other methodologies. This substantiates that the model parameters from ETM are highly affected by the AIF.

Table 4.3: A summary of the median K^{trans} , k_{ep} , v_e and v_p derived from extended Tofts' method when using different methods for estimating the arterial input function. The range of the values are included in parenthesis. K^{trans} and k_{ep} have the unit min^{-1} , while v_e and v_p are fractions of total tissue volume inside a voxel.

	Manual AIF (n=20)	Population-based AIF (n=20)	Semi-automatic AIF (n=18)
K^{trans}	0.13 (0.047 - 0.41)	0.10 (0.042 - 0.24)	0.11 (-0.035 - 1.59)
k_{ep}	0.58 (0.047 - 1.97)	0.43 (0.088 - 1.97)	0.61 (-0.65 - 2.24)
v_e	0.26 (0.081 - 0.99)	0.25 (0.050 - 0.99)	0.47 (0.00036 - 0.99)
v_p	0.21 (0.073 - 0.33)	0.21 (0.064 - 0.37)	0.37 (1.06×10^{-9} - 0.63)

Figure 4.7 shows Bland-Altman plots comparing the derived K^{trans} values from ETM when different methods for estimating the AIF were used.

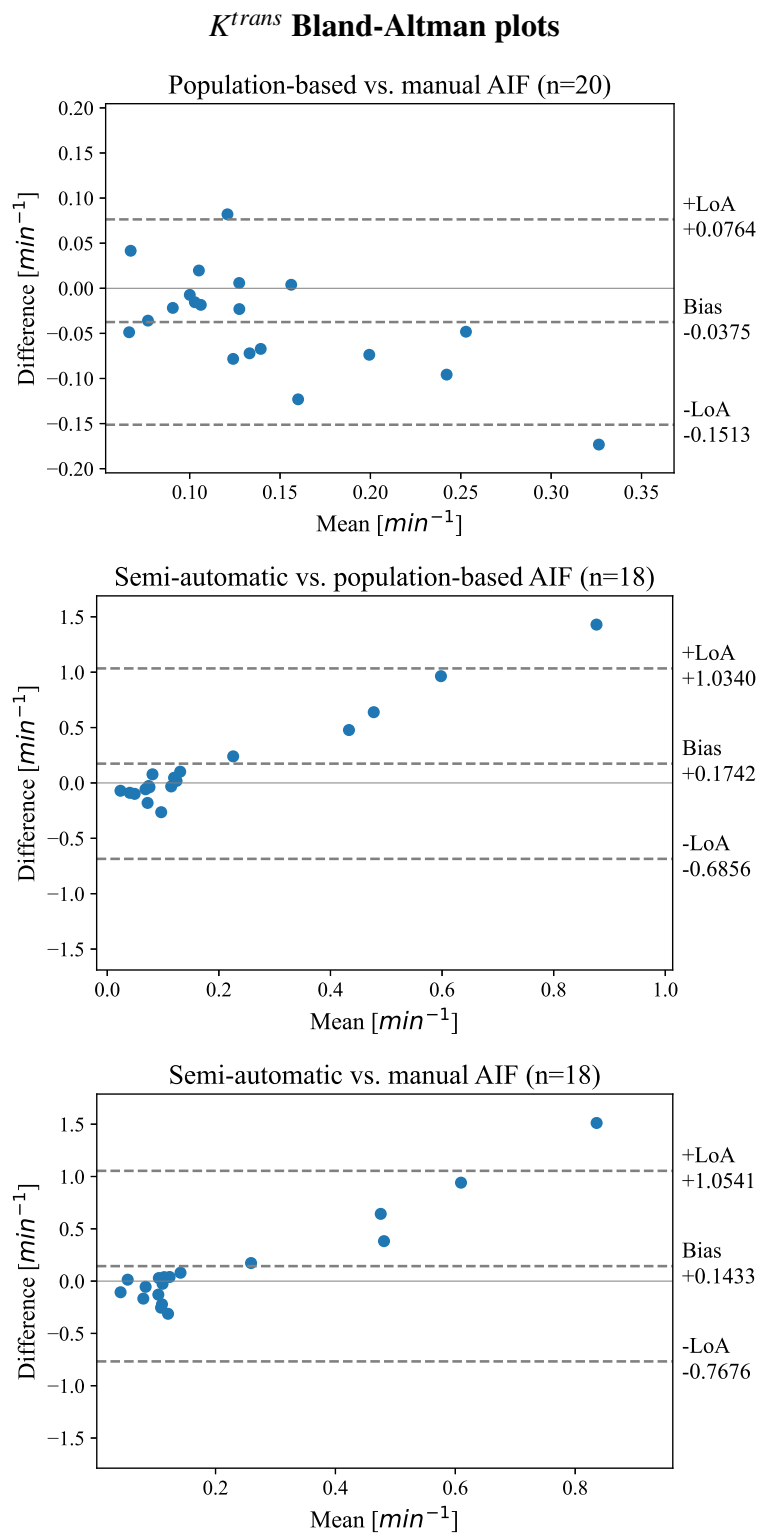


Figure 4.7: Bland-Altman plots of the derived K^{trans} values from extended Tofts' method, comparing three different arterial input function (AIF) methods, illustrating that the semi-automatic AIF approach results in more outliers in the derived K^{trans} values. The axes of the plots have different ranges and LoA represents the upper and lower limits of agreement.

From Figure 4.7 it is observed from the bias that the manual AIF method on average measures 0.0375min^{-1} (21.8%) higher K^{trans} values than the population-based AIF method. The semi-automatic AIF method measures higher K^{trans} values than both the population-based AIF method and the manual AIF method, on average. This is illustrated by the biases in Figure 4.7. The semi-automatic AIF method seems to produce some outliers in the model parameters derived from ETM, which is observed from some of the points in the plot and the upper and lower LoAs. This illustrates that the model parameters are affected by the input plasma concentration, which is based on the AIF.

The plots illustrated in Figure 4.8 are all based on the same patient data. The plots illustrated to the left and right in the figure are based on data from the same patients, respectively. Three different AIF methodologies were used for generating the plots in Figure 4.8. These plots show tissue signal intensity curves estimated with ETM. The ETM curves are plotted together with the signal intensity curves in the tissue of interest and the plasma signal intensity. The plasma signal intensity curves were derived from the AIF curves.

Figure 4.8 shows six plots where all of the left plots are based on data from a patient where the AIF was relatively easy to annotate manually and the annotated AIF ROI was made up of several voxels (left image and plot in Figure 4.1 in section 4.1.1). The right plots in Figure 4.8 are based on data from a patient where the AIF was more difficult to annotate manually and the annotated AIF ROI was only comprised of a few voxels (right image and plot in Figure 4.1 in section 4.1.1). From Figure 4.8 we can see that the right AIF curve derived from the semi-automatic AIF methodology is characterized by a lot of noise and does not have a clear peak value. As a consequence, the estimated signal intensity from ETM becomes more noisy. Contrarily, the left plot derived from the semi-automatic AIF method has a clear peak value and less noise. The two minutes post-CA injection break is observed in the curves around the time between 100 and 200 seconds into the imaging sequence.

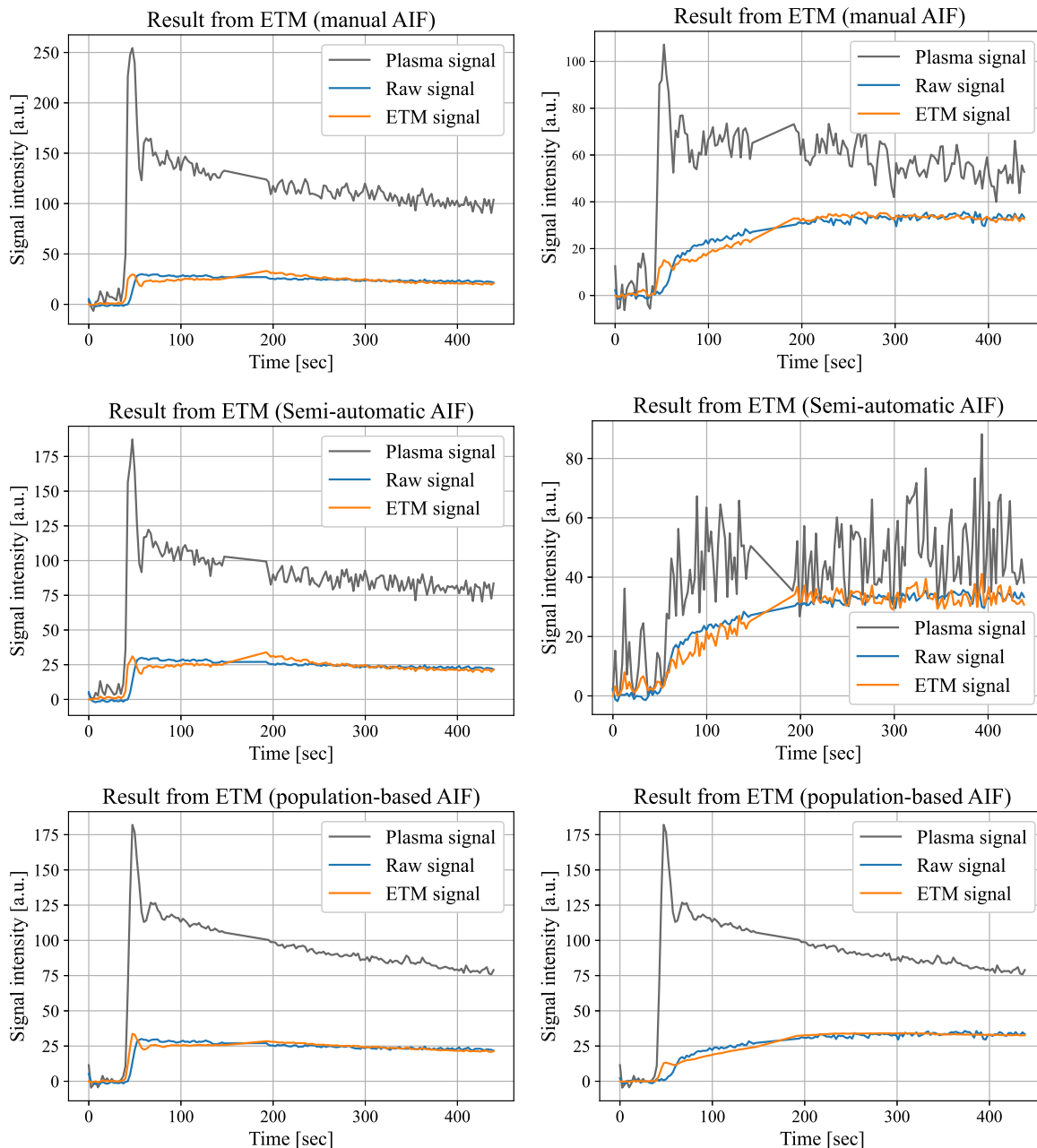


Figure 4.8: The tissue signal intensity estimated by extended Tofts' method plotted together with the mean signal intensity inside the tumor and the plasma signal intensity. In the plots, the raw signal illustrates the signal intensity curves in the tissue of interest before modeling. The plots are based on data from two different patients. All of the plots to the right are based on the same patient data, while the plots to the left are based on the same patient data.

The K^{trans} values derived from ETM when using the manual AIF method and the population-based AIF method are positively correlated (p-value < 0.05). Contrarily, the K^{trans} values derived from ETM using the semi-automatic AIF method and the manual AIF method are slightly negatively correlated and the correlation is not statistically significant (p-value > 0.05). When the correlation between the K^{trans} values from

ETM using the population-based AIF method and the semi-automatic AIF method was tested a slightly positive correlation was observed, but it is not statistically significant (value > 0.05). All of the calculated Spearman correlation coefficients and p-values can be found in Appendix A.3.1.

The Wilcoxon signed-rank test gives statistically significant evidence to reject the null hypothesis for the K^{trans} parameters from ETM using the manual AIF method and the population-based AIF method. This means that we accept that the median K^{trans} values are different (p-value < 0.05). When testing the null hypothesis for the K^{trans} values from ETM when using the semi-automatic AIF method with the parameters from the two other methodologies, the Wilcoxon signed-rank test gives statistically significant evidence to accept the null hypothesis (p-value > 0.05). This substantiates that the median value of the semi-automatic AIF method is similar to the median values of the two other AIF methods, even though the mean values are different. The median K^{trans} value from the semi-automatic AIF method is 0.1093min^{-1} , which is lower than the mean K^{trans} value of 0.291min^{-1} . This illustrates that the model parameters from ETM when using the semi-automatic AIF method are affected by outliers. The p-values calculated from the Wilcoxon signed-rank test can be found in Appendix A.3.2

Erosion and dilation of tumor masks

Table 4.4 shows the median model parameters from ETM when doing an erosion and a dilation of the tumor masks. From Table 4.4 it is observed that the model parameters derived from ETM were not affected too much when the whole-volume tumor masks were made smaller and larger.

Table 4.4: Median of the derived parameters from extended Tofts' method when using a population-based arterial input function and doing an erosion and a dilation of the tumor masks ($n=20$). v_e and v_p are fractions of the total tissue volume inside a voxel, while K^{trans} and k_{ep} are in units of min^{-1} .

	Original mask	Eroded mask	Dilated mask
K^{trans}	0.10 (0.042 - 0.24)	0.11 (0.043 - 0.25)	0.11 (0.052 - 0.28)
k_{ep}	0.43 (0.088 - 1.97)	0.50 (0.10 - 2.45)	0.50 (0.079 - 2.03)
v_e	0.25 (0.050 - 0.99)	0.22 (0.044 - 0.99)	0.26 (0.056 - 0.99)
v_p	0.21 (0.064 - 0.37)	0.20 (0.067 - 0.36)	0.21 (0.065 - 0.41)

Parameter maps

Figure 4.9 illustrates parameter maps of the derived perfusion parameters from a single slice obtained from the data of one patient. K^{trans} , k_{ep} , v_e and v_p are here illustrated for data inside the tumor, while the rest of the voxels are zero. The parameter maps present the variations in the derived model parameters visually.

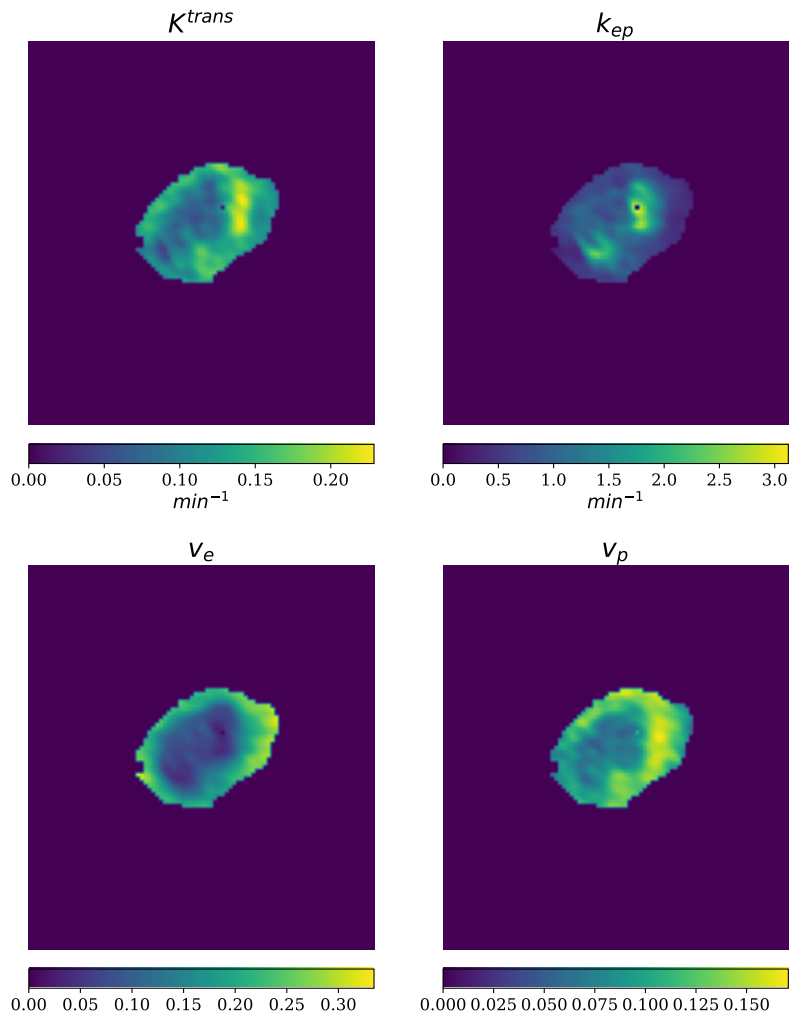


Figure 4.9: Parameter maps of the parameters K^{trans} , k_{ep} , v_e and v_p derived from extended Tofts' method when using a manually annotated arterial input function. v_e and v_p are fractions of the total tissue volume inside a voxel.

4.2.2 Modeling in the research information system

Table 4.5 shows the mean model parameters from ETM when utilizing the research information system and using a population-based AIF (n=63). The population-based AIF method was chosen mainly due to the high time consumption in manually annotating the AIFs and due to the varying performance of the automatic AIF.

Table 4.5: A summary of the mean parameters from extended Tofts' method when using a population-based AIF (n=63). The differences between the results from average and voxelwise modeling are included in the bottom row. v_e and v_p are fractions of the total tissue volume inside a voxel, while K^{trans} and k_{ep} are rates in min^{-1} .

	K^{trans}	k_{ep}	v_e	v_p
Average	0.178 ± 0.121	0.669 ± 0.521	0.339 ± 0.211	0.204 ± 0.107
Voxelwise	0.190 ± 0.127	0.817 ± 0.547	0.379 ± 0.179	0.203 ± 0.106
Difference	0.0122 (6.67%)	0.147 (19.85%)	0.0399 (11.08%)	0.00120 (0.59%)

Table 4.6 shows the median of the derived model parameters from ETM (n=63) when modeling based on the average signal intensity inside the tumor. The median of the derived parameters from modeling based on the average signal intensity are all slightly lower than the mean of the derived parameters.

Table 4.6: The median model parameters from extended Tofts' method when using a population-based AIF (n=63). Only the parameters derived from modeling based on the average signal intensity inside the tumor are included. K^{trans} and k_{ep} have the unit min^{-1} , while v_e and v_p are fractions of total tissue volume inside a voxel.

	Median (range)
K^{trans}	0.163 (0.025 - 0.923)
k_{ep}	0.531 (0.0258 - 3.173)
v_e	0.283 (0.048 - 0.999)
v_p	0.195 (~0 - 0.545)

Figure 4.10 shows the differences in the derived K^{trans} values from average and voxelwise modeling, plotted against the tumor volume (n=63). From Figure 4.10 it is observed that most patients had a tumor volume < 30 ml and only 6 out of 63 patients had a tumor volume > 30 ml. The differences in the derived K^{trans} values do not seem to be correlated with tumor volume from what is observed in Figure 4.10.

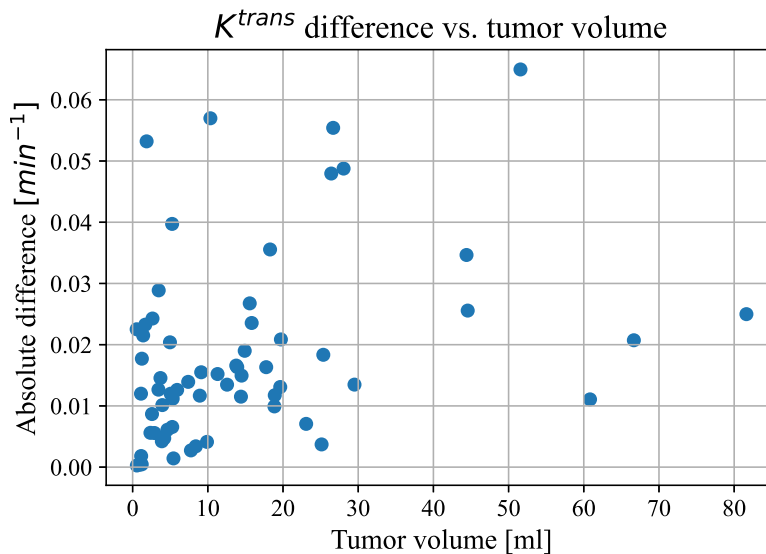


Figure 4.10: Differences in K^{trans} (min^{-1}) values from Extended Tofts' model when modeling based on the average signal intensity and modeling based on the voxelwise signal intensity inside the tumor ($n=63$). No specific coherence seems to be present between the K^{trans} differences and tumor volumes.

Figure 4.11 shows a Bland-Altman plot of the derived K^{trans} parameters ($n=63$). This figure compares the parameters derived when modeling based on the average signal intensity inside the tumor with the parameters derived when modeling based on the voxelwise signal intensity. The bias is -0.012min^{-1} indicating that the voxelwise method on average measures a 0.012min^{-1} (7.0%) higher K^{trans} than the average method.

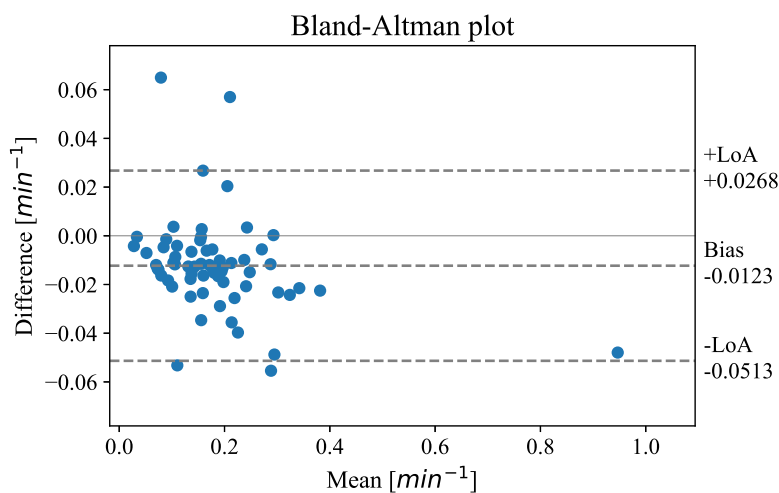


Figure 4.11: Bland-Altman plot of the K^{trans} parameters from extended Tofts' method, illustrating the differences between the derived K^{trans} values when modeling based on the average signal intensity and modeling based on the voxelwise signal intensity inside the tumor ($n=63$). A population-based arterial input function was used. +LoA and -LoA represent the upper and lower limits of agreement.

The K^{trans} parameters derived from the average and voxelwise modeling methods are positively correlated and the correlation is statistically significant (p-value $\ll 0.05$). This is in agreement with what was observed in section 4.2.1 when comparing the results from average and voxelwise modeling when modeling was done in the local modeling environment. The Spearman correlation coefficients and the p-values can be found in Appendix A.3.1.

The Wilcoxon signed-rank test indicates that the median is different between the K^{trans} parameters derived from ETM when modeling based on the average signal intensity and modeling based on the voxelwise signal intensity ($p < 0.05$). The null hypothesis stating that the median difference between the model parameters is zero is rejected by the Wilcoxon signed-rank test. The calculated median K^{trans} values from the average modeling method and the voxelwise modeling method are 0.163min^{-1} and 0.171min^{-1} , respectively. The calculated p-value can be found in Appendix A.3.2.

4.3 Correlation with histologic tumor grade

The obtained model parameters derived from ETM, through the utilization of the research information system, were analyzed for correlations with histologic tumor grade. Table 4.7 shows a summary of the parameters derived from ETM for low-risk and high-risk histologic grades (n=60). Only model parameters from 60 patients were analyzed because the histologic tumor grades were missing for three patients. From Table 4.7, no prominent differences are observed between the median model parameters for the low-risk and high-risk tumor grades.

Table 4.7: The median of the derived parameters from extended Tofts' method summarized for low-risk and high-risk histologic tumor grade. The range of the values is added in parentheses. v_e and v_p are fractions of total tissue volume inside a voxel, while K^{trans} and k_{ep} are in units of min^{-1} .

	Low-risk (n=40)	High-risk (n=20)
K^{trans}	0.157 (0.026 - 0.923)	0.164 (0.048 - 0.312)
k_{ep}	0.494 (0.026 - 3.173)	0.563 (0.153 - 1.417)
v_e	0.230 (0.048 - 0.999)	0.276 (0.087 - 0.826)
v_p	0.187 (~ 0 - 0.545)	0.203 (0.112 - 0.462)

Figure 4.12 shows ROC curves of the derived K^{trans} , k_{ep} , v_e and v_p values, respectively. This plot shows whether there is any correlation between the parameters derived

from ETM and the histologic tumor grade. The histologic grade is defined to be 0 for low-grade cancers and 1 for high-grade cancers. All of the plots show no correlation between the derived perfusion parameters and histologic tumor grade.

ROC curves

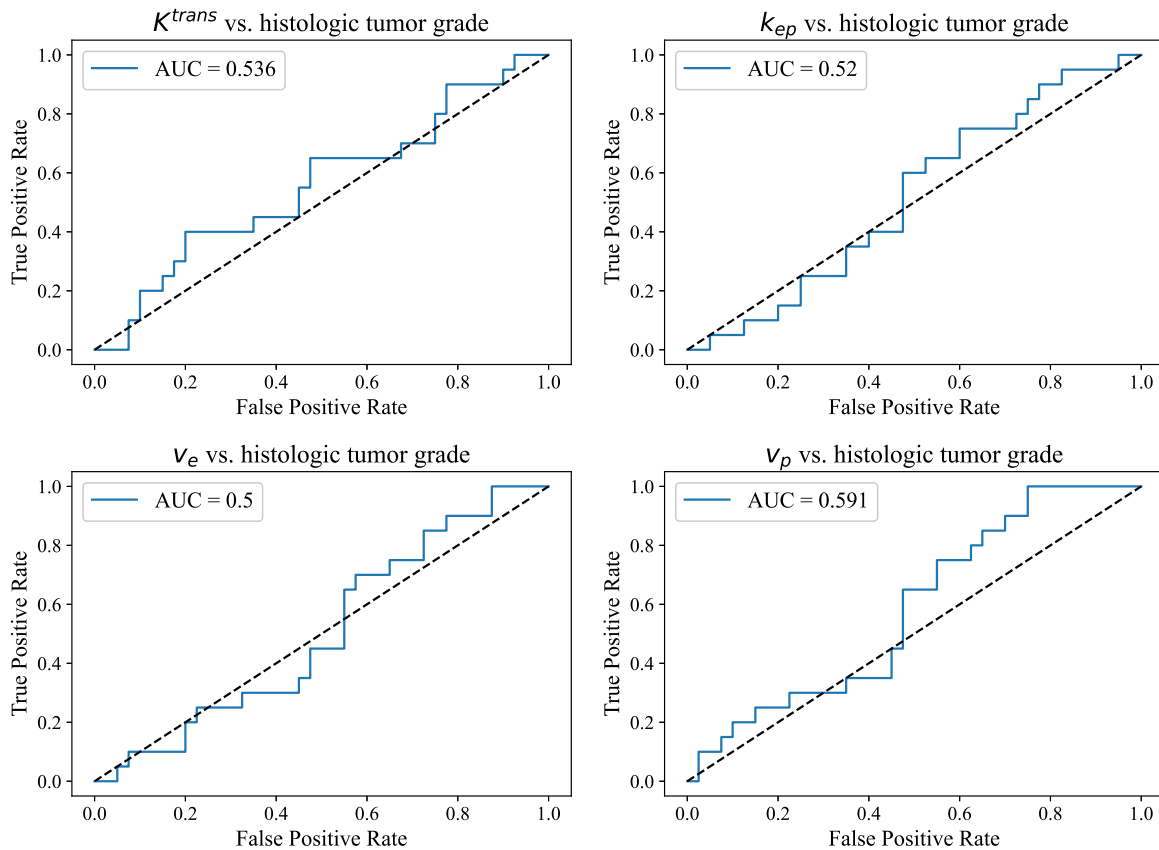


Figure 4.12: Receiver operating characteristics (ROC) curves, where it is analyzed whether there is a correlation between the derived model parameters and histologic tumor grade ($n=60$). The histologic tumor grade is divided into low-risk and high-risk tumor grades. No correlation is observed from this figure.

A chi-square test gave p-values of 0.232 and 0.157 for the low-risk and high-risk histologic subtypes, respectively. This indicates that there is evidence to reject the null hypothesis, which states that the histologic grades have given frequencies, which was based on splitting the derived K^{trans} values by the median value. This means that no correlation was observed between the derived perfusion parameters and histologic tumor grade from the chi-square test.

Chapter 5

Discussion

The main purpose of this project was to estimate quantitative perfusion parameters that might be related to the biology of endometrial carcinomas. DCE-MRI data from patients diagnosed with endometrial cancer were analyzed for this purpose. Four main objectives were listed in the introduction of this thesis, including implementing ETM in Sectra research PACS, testing ETM for both average and voxelwise modeling, and for different AIF methods, and last but not least comparing the results with values from the literature and analyzing for correlation with clinical parameters. ETM was implemented in Python and three different methods for estimating the AIF were tested on data from 20 patients in a local modeling environment. The parameters derived from ETM when using different AIF methods and from average and voxelwise modeling were then compared. ETM was also implemented in the research information system where the model was tested on data from 63 patients using a population-based AIF. The presence of correlations between the model parameters derived from the research environment and the histologic tumor grade was investigated. In this chapter, we compare the derived model parameters with values from the literature and discuss the findings and the limitations of the project. Suggestions for future work are presented at the end of the chapter.

5.1 The Arterial Input function

A precise AIF is important in quantitative models where the plasma concentration is required as an input. In this project, it was illustrated that the input plasma concentration affects the derived model parameters. Three different methods for estimating

the AIF were implemented in this project, including manual annotation of the AIF, a semi-automatic algorithm and a population-based AIF.

Hematocrit of 42% was assumed for all patients when calculating the plasma concentration, but this number will in fact vary between patients. The input plasma concentration is in reality supposed to be the concentration of plasma in an artery that is feeding the tissue of interest, which in this case is the uterus. In this project, the AIF was estimated by finding the concentration of CA in the iliac arteries or in the aorta. Other errors may occur in the cases where the AIF was estimated from the aorta. Since the AIF in theory is supposed to be feeding the tissue of interest, the aorta is most likely further away from the tissue of interest than the iliac arteries and might therefore be a poorer estimate of the AIF. However, when the AIF was estimated from the aorta a larger ROI was possible to obtain. Less noise and a higher peak value were observed when the AIF was estimated from the aorta, which may be because a bigger ROI was possible to obtain in the aorta. It is unclear what aspect affects the resulting model parameters the most.

Based on the results from the three methods for estimating the AIF it seems like the population-based AIF is the method that is most robust in this project. The mean and median model parameters from ETM when using the population-based AIF are closest to the literature values between the three methods. It was observed that the manual AIFs consist of more noise, especially when the desired artery consists of few voxels, which was the case for several patients. The semi-automatic algorithm for estimating the AIF did not perform well for data from several patients, especially when the desired artery was comprised of few voxels in the DCE-MRI images. The algorithm failed to find an AIF for 17, 7 and 2 out of 20 patients when choosing 1%, 2% and 3% brightest voxels in the first step of the algorithm, respectively. Therefore, the population-based algorithm seems to be the most robust way of finding the AIF from what was observed in this project. However, all of the AIF methodologies have some limitations.

5.1.1 The manually annotated AIF

AIFs were annotated manually on data from 20 patients in the local modeling environment. A variation was observed in the difficulty of manually annotating AIFs from the DCE-MRI images. Selection bias might be present, because tissue outside the artery

may be included in the annotated ROIs. All of the selected voxels might not be inside the desired artery. For certain patients, the artery consisted of multiple voxels. For these patients, the AIF curve had a high first peak, a longer washout period and relatively little noise. Other patients had an artery consisting of only a few voxels making it difficult to annotate the AIF. These assumptions were made by visually examining the DCE-MRI images and the resulting AIF curves. Figure 4.1 (section 4.1.1) shows images from two patients illustrating how different the DCE-MRI images look between patients and how the AIF curves are affected by the annotated AIF ROIs. It is likely that the discrepancies in the data arise from variations in anatomy between the patients. The coordinate system of the MRI machine is changed to fit the location of the uterus, hence the location of the slices differs between the patients. The arteries are sliced in different ways depending on the anatomy of the patient and the location of the slices.

The AIF annotations were only performed on one slice. The resulting AIFs might have been more accurate if the annotations were performed on several slices where the CA was observed in the desired artery. It should also be mentioned that the annotations were carried out by a person with limited knowledge in female pelvic anatomy. An experienced radiologist might have been able to make more precise annotations of the AIF from the DCE-MRI images. Human errors might consequently affect the AIF annotations.

5.1.2 The semi-automatic AIF

A semi-automatic algorithm for estimating the AIF was implemented in the local modeling environment. The algorithm did not manage to find an AIF for all of the 20 patients that it was tested on. The DCE-MRI data exhibit great variations, all DCE-MRI images look different, the FOV varies and the resolution is not too good. The DCE-MRI images are also sensitive to patient movement. These are all possible contributors to the diverse results from the semi-automatic AIF algorithm.

The semi-automatic algorithm seems to select the areas of the DCE-MRI image that are relevant in the first step of the algorithm presented in section 2.4.2. This means that the algorithm fails in some later step. 20 time steps seem to be sufficient to cover the arrival time for the CA. This evaluation is based on manually analyzing the DCE-MRI images when the AIF annotations were carried out. The algorithm seems to fail at

the sixth step when visually looking through the output from the different steps of the algorithm. The fourth and fifth steps of the algorithm were not included. These steps include filtering and were not included as the desired artery might not be tubular due to the different locations of the slices in the DCE-MRI images. However, the output from the algorithm might be affected by the decision to not include filters.

If more time had been invested in developing an automatic algorithm for finding the AIF, it might have been possible to tailor the algorithm better to endometrial cancer data and develop an algorithm with better performance. It could be relevant to check the orientation of the data in order to tailor the algorithm to different orientations of DCE-MRI data.

5.1.3 The population-based AIF

The population-based AIF consists of less noise than the manually annotated AIFs and the semi-automatic AIFs. This might be due to a smoothing effect from calculating the mean from annotated AIFs from 20 patients. Even though the contrast was administered at the same time for all patients, the contrast will most likely arrive in the artery at different times. This is due to different cardiovascular functions and the ability to deliver blood to the microvascular tissues between the patients. Additionally, the magnitude of the peak of the AIF curve differs between patients and was not tailored to the individual patient data. The population-based AIF was not tailored to the data from each specific patient, which may affect the resulting model parameters.

5.2 Extended Tofts' Method

ETM was used for analyzing DCE-MRI time-series data from endometrial cancer patients. Two MRI images were required for running the model, including the DCE-MRI image and the whole-volume tumor mask. Using these two MRI images, modeling was performed on data inside the tumor. The segmentation of tumor masks on one MRI image and the subsequent modeling on a different MRI image introduces a source of uncertainty. Artefacts may occur due to the co-registration of the two images. The dimensions of the tumor masks were changed to fit the dimensions of the dynamic images, which may lead to registration artefacts. If segmentations were performed

directly on the DCE-MRI images this could have been avoided. However, other limitations might be present when annotating tumor ROIs directly on the DCE-MRI data. For instance, the resolution of the DCE-MRI images is often poorer than the resolution of the structural MRI images, which may increase the difficulty in manually segmenting tumor ROIs on the DCE-MRI images.

DCE-MRI images might be affected by motion artefacts, hence motion correction could have been implemented for all DCE-MRI images. Motion correction using MCFLIRT from FSL was tested, but not implemented further [54]. It was decided to not use motion correction further because no particular changes were observed in the derived parameters when motion correction was applied to the DCE-MRI time-series data before modeling. However, motion correction was only tested on data from two patients and it might have improved the results when analyzing data from other patients. In addition, the tool tested for motion correction is provided by FSL, which is an analyzing tool mainly developed for brain imaging data [54]. This might be a reason for the tool not working as well for endometrial cancer data.

5.2.1 Comparing average and voxelwise modeling results

Two different ways of modeling were tested in the present project. Firstly, modeling was performed based on the average signal intensity inside the tumor. Secondly, modeling was performed based on the voxelwise signal intensity inside the tumor and calculating the average model parameters afterwards. These two modeling configurations were compared to check whether there are any prominent differences between the two ways of modeling. Since whole-volume tumor masks were utilized in this project, selection bias might be present if all of the voxels making up the tumor masks do not solely consist of tumor tissue. An assumption is made about the tissue compartments of the voxels in ETM, which might not necessarily be the case for a particular voxel. In addition, the AIF should be the CA concentration from an artery that is feeding the tissue of interest. For the voxelwise approach, the AIF should ideally be feeding the particular voxel, which is not the case.

Results from ETM using all AIF methods indicate that the voxelwise modeling method on average measures a slightly higher K^{trans} value than the average method. This is shown from the bias in the Bland-Altman plots comparing the results from average and

voxelwise modeling (Figures 4.5 and 4.11 in sections 4.2.1 and 4.2.2, respectively). The mean differences in K^{trans} are however so small that it is unclear if this result is systematic. The biggest absolute mean difference between the K^{trans} values from the two ways of modeling was observed for the population-based AIF method (Table 4.1 in section 4.2.1). This can come from the population-based AIF being more smooth than the other AIFs introducing scaling effects. If the population-based AIF is more accurate than the two other AIF methods, the difference between the average and voxelwise modeling results might become more prominent. The mean absolute differences were calculated here, and the calculated absolute mean differences might be affected by outliers.

Positive correlations were observed between the K^{trans} parameters derived from the average and voxelwise modeling methods for all AIF methods and the positive correlation is statistically significant. However, Spearman's correlation coefficient only measures if a correlation is present and not if the values are similar between the two groups of model parameters.

The median is different between the K^{trans} parameters derived from the average and voxelwise modeling methods for the population-based AIF method from the Wilcoxon signed-rank test. Contrarily, the median is similar between the K^{trans} parameters derived from the average and voxelwise modeling methods for the manual AIF method and the semi-automatic AIF methods. The mean and median K^{trans} values from the average and voxelwise modeling methods were less similar when the population-based AIF method was used than the mean and median K^{trans} values derived from average and voxelwise modeling when the two other AIF methodologies were used.

The differences in the derived K^{trans} values from modeling based on the average signal intensity and from modeling based on the voxelwise signal intensity indicate that more outliers are observed for the semi-automatic AIF method (Figure 4.4 in section 4.2.1). The larger differences observed for this AIF method might also be due to generally larger model parameters derived from this AIF method, as illustrated from the calculated mean values (Table 4.1 in section 4.2.1).

More variations were observed in the derived k_{ep} values from average and voxelwise modeling (Table 4.1 in section 4.2.1). Therefore, the derived k_{ep} values were plotted against the tumor volume to look for possible relations (Figure 4.6 in section 4.2.1). There does not seem to be a connection between the tumor volume and the variations in

the k_{ep} values between the two methods. However, for the semi-automatic AIF method, there are some larger values that seem to be outliers affecting the mean k_{ep} values. The outliers are mostly observed in the k_{ep} parameters derived from modeling based on the voxelwise signal intensity at low tumor volumes. This might indicate that a voxel is too small introducing errors. When summing up the results from all voxels we might calculate accumulated errors. It might also indicate that for small tumors, some voxels outside of the tumor are included making the resulting k_{ep} values differ from the rest.

The variations between the v_p values derived from average and voxelwise modeling are small (Table 4.1 in section 4.2.1). A slightly higher deviation was observed between the derived v_e values. v_e , K^{trans} and k_{ep} are dependent, which might be a reason for the slightly higher mean absolute differences observed in this variable, leading to outliers in the derived v_e values as well.

5.2.2 Modeling results from different AIF methods

The parameters derived from ETM when using different methods for estimating the AIF were compared. The mean absolute differences between the derived parameters are quite high (Table 4.2 in section 4.2.1). The large absolute differences in the derived perfusion parameters substantiate that the AIF affects the parameters derived from ETM a lot. The largest mean absolute differences in the derived perfusion parameters were observed when comparing the model parameters from the semi-automatic AIF method with the model parameters from the two other methodologies. Since the absolute mean differences were analyzed here, the resulting differences might be affected by outliers.

The resulting parameters derived from ETM were not normally distributed, so the median of the derived model parameters was tabulated as well (Table 4.3 in section 4.2.1). It was observed that the median of the derived parameters was more similar between the different AIF methodologies. However, the ranges in the derived model parameters were observed to be larger for the semi-automatic AIF method, which also shows that this AIF method is affected more by outliers than the other AIF methods in the present project.

Bland-Altman plots were created for comparing the K^{trans} values from the different AIF methods (Figure 4.7 in section 4.2.1). The manual AIF method measures higher K^{trans} values than the population-based AIF method on average ($\sim 22\%$). The deviations

in the derived model parameters might come from the smoothness of the AIF curves. The smoothness of the AIF curves affects the smoothness of the signal intensity curve obtained from ETM (Figure 4.8 in section 4.2.1). The manual AIFs were affected more by noise, especially when the desired artery was small and difficult to see in the DCE-MRI images resulting in a small AIF ROI. The population-based AIF was not fitted to the data from each patient. The arrival time and signal intensity of the CA might differ between patients. Hence, the parameters might be affected by the location and the magnitude of the peak in the population-based AIF. These are possible contributors to the deviations in the results from the population-based and the manual AIF methods.

The semi-automatic AIF method produced more outliers in the derived model parameters, which is illustrated in the K^{trans} Bland-Altman plots (Figure 4.7 in section 4.2.1). It was observed that the semi-automatic AIF method resulted in AIF curves with higher levels of noise and no distinct peak values when data from several patients were analyzed (Figure 4.8 in section 4.2.1). This might affect the derived model parameters and may be a reason for the high deviation in the results from the semi-automatic AIF method compared to the results from the other methodologies.

A positive correlation was observed between the derived K^{trans} values from the manual AIF method and the population-based AIF method from Spearman's rank correlation coefficient. Contrary, no statistically significant correlations were observed between the derived K^{trans} values from the automatic AIF method and the two other methodologies when Spearman's rank correlation coefficient was calculated.

The median K^{trans} values from the manual AIF method and the population-based AIF method are statistically significantly different from the Wilcoxon signed-rank test. However, the Wilcoxon signed-rank test gives evidence to accept that the median K^{trans} from the semi-automatic AIF method is similar to the median K^{trans} from the two other AIF methods. Initially, it may appear weird that the median K^{trans} obtained from ETM when using the automatic AIF exhibits the highest similarity to the median K^{trans} derived from the other two methodologies. However, the Wilcoxon signed-rank test is robust to outliers, which was mostly observed in the results from the semi-automatic AIF method. This indicates that, excluding the outliers obtained from the semi-automatic AIF method, the remaining parameters align more with the model parameters obtained from the other two AIF methodologies.

In this project, the semi-automatic AIF seems like the least robust AIF method, leading

to outliers in the derived model parameters, even though the median K^{trans} value is similar to that of the two other methods for estimating the AIF. The derived perfusion parameters seem to be affected when the algorithm fails in estimating an AIF curve shaped with a high first peak value, a longer washout period and little noise. In this project, it was observed that the population-based AIF seems to be the most robust method for estimating the AIF. This evaluation is both based on the resulting parameters from ETM and the time consumption and difficulty in manually annotating AIFs from DCE-MRI data.

5.2.3 Erosion and dilation of tumor masks

Erosion and dilation of the whole-volume tumor masks were tested for the population-based AIF method when modeling in the local environment. This was done as a test of whether the tumor masks were correctly aligned with the tumor after performing a co-registration between the tumor masks and the DCE-MRI images. Research have indicated higher K^{trans} values in the myometrium [1][12]. If normal myometrium is present in the tumor masks we might expect the K^{trans} values to be higher. For this reason, erosions and dilations were tested to get an estimation of whether tissues outside of the tumor were present in the tumor masks after co-registration. Both erosion and dilation barely changed the derived K^{trans} values (Table 4.4 in section 4.2.1). This indicates that the tumor masks consist of mostly tumor tissue after co-registration. A double erosion was also tested, but for small tumor masks, there were zero true voxels left in the image, and modeling could not be performed.

5.2.4 Parameter maps

Parameter maps were created based on the model parameters derived from ETM when using a manually annotated AIF (Figure 4.9 in section 4.2.1). The parameter maps show voxelwise modeling results, where all voxels outside the tumor are zero. There are also some areas inside the tumor where the values are zero because the maximum number of function evaluations was reached. For these voxels, the model was not able to find perfusion parameters before a set number of function evaluations were reached. The reason for the optimization not working for all of the voxels inside the tumor is unclear, but might be connected to the tissue compartments of the prospective voxels.

If the voxels do not consist of the compartments assumed from ETM, errors may occur. The parameter maps show visually where in the tumor the derived perfusion parameters are higher and lower, and might serve as a tool for radiologists when they evaluate MRI images.

5.2.5 Comparison with values from the literature

Three studies were chosen as a basis for comparison. Two of the studies have used almost the same model as we have in this project, while one of the studies used a different two-compartment pharmacokinetic model to derive similar parameters [1][12][13].

Fasmer et al. used ETM to analyze DCE-MRI data from endometrial cancer patients in nordicICE (Nordic-NeuroLab AS, Bergen, Norway) [12]. The data analyzed by Fasmer et al. were derived from the same cohort as the data analyzed in the present study. They found K^{trans} , k_{ep} and v_e values that are lower than the median parameters derived in this project (median values: $K^{trans} = 0.034min^{-1}$, $k_{ep} = 0.40min^{-1}$, $v_e = 9\%$) (n=177). They found higher K^{trans} , k_{ep} and v_e values in the normal myometrium (median values: $K^{trans} = 0.086min^{-1}$, $k_{ep} = 0.42min^{-1}$, $v_e = 21\%$). Fasmer et al. annotated tumor ROIs directly on the DCE-MRI images in 2D to avoid registration artefacts and used a population-based AIF calculated by the nordicICE software [12].

Haldorsen et al. analyzed contrast concentration curves in the myometrium and in the endometrial cancer regions using the adiabatic approximation model of Johnson and Wilson (aaJW) [1]. From this model, they derived parameters reflecting the tissue microvasculature. They derived K^{trans} , k_{ep} , V_e and V_p among other parameters. Even though Haldorsen et al. used a different model, there might be a foundation for comparison since they derived the same parameters and analyzed data from the same cohort as we did in this project. Haldorsen et al. found lower K^{trans} and k_{ep} values than what was observed in the present project (mean values: $K^{trans} = 0.026min^{-1}$, $k_{ep} = 0.30min^{-1}$) (n=55). Haldorsen et al. did not find higher k_{ep} values in the normal myometrium like Fasmer et al. did, but they did find higher K^{trans} values in the normal myometrium (mean value: $0.06min^{-1}$) than in the cancer tissue. Haldorsen et al. annotated tumor ROIs directly on the DCE-MRI images similar to Fasmer et al. [12]. They also annotated an ROI in the normal myometrium and in a feeding artery. Due to the poor quality of the AIF ROI, they decided to use a population-based vessel signal that was

optimized for the individual patients [1].

In addition to optimizing model parameters in the endometrial cancer tissue and in the normal myometrium, Haldorsen et al. looked at the differences between the model parameters in the endometrioid and non-endometrioid cancer types [1]. They found slightly higher K^{trans} and k_{ep} values in the endometrioid histologic type (mean values: $K^{trans} = 0.027min^{-1}$, $k_{ep} = 0.31min^{-1}$), than what they did for the non-endometrioid histologic type (mean values: $K^{trans} = 0.022min^{-1}$, $k_{ep} = 0.26min^{-1}$). However, Haldorsen et al. found no significant differences in the perfusion parameters among the tumor grades [1].

Ye et al. analyzed DCE-MRI data from endometrial cancer patients using two different models, the extended Tofts' method (ETM) and the distributed parameter (DP) model [13]. From ETM they found higher K^{trans} and k_{ep} for low-risk type endometrial cancer (median values: $K^{trans} = 0.10min^{-1}$, $k_{ep} = 1.20min^{-1}$) than they did for high-risk type endometrial cancer (median values: $K^{trans} = 0.05min^{-1}$, $k_{ep} = 0.57min^{-1}$) (n=51). The median K^{trans} values obtained in the present project are higher than the median K^{trans} values derived by Ye et al. in both of the histologic types (Table 4.6 in section 4.2.2). Contrarily, we found a slightly lower median k_{ep} value than what was observed by Ye et al. in both of the histologic types. Ye et al. used individually annotated AIFs from the iliac arteries. They used commercially available software (Mltalytics, FITPU Healthcare, Singapore) to extract DCE-MRI parameters [13].

The three studies chosen as a basis for comparison have all calculated lower K^{trans} values than we have in this project. Fasmer et al. also calculated lower v_e values for the cancer tissue than what was derived in the present project [12]. Ye et al. calculated higher k_{ep} values than we did in the present project, while Fasmer et al. and Haldorsen et al. derived lower k_{ep} values than the derived k_{ep} values in this project. The differences between the parameters derived in this project and the parameters derived in the three other studies might be influenced by methodological reasons, as different methods were used to extract parameters from ETM. In addition, Haldorsen et al. used a different compartmental model [1]. ETM might have been implemented differently and optimization might have been performed in a different manner by Fasmer et al. and Ye et al. than in the present study [12][13].

The three studies also used different methods for estimating the AIF [1][12][13]. The findings in this project illustrate that the model parameters from ETM are highly in-

fluenced by the estimated AIF. The AIF seems to be the one input parameter that influences the resulting model parameters from ETM the most. The present study has shown that the choice of AIF influences the derived model parameters and might be a reason for the deviations in the derived parameters between the studies.

In all of the three studies used as a basis for comparison, tumor masks were annotated directly on the DCE-MRI images [1][12][13]. In this project, whole-volume tumor masks were used and a co-registration was performed between the tumor masks and the DCE-MRI images. This might lead to differences in the obtained model parameters. The way in which MRI signal to CA concentration conversion is handled might also differ and influence the derived perfusion parameters. Differences between the MRI machines and imaging protocols might also influence the dynamic MRI acquisitions and hence the derived perfusion parameters.

5.2.6 Correlation with histologic tumor grade

An investigation was carried out to determine if there exists any correlation between the derived model parameters and the histologic tumor grade. The histologic tumor grades analyzed in this project were divided into low-risk and high-risk histologic grades. ROC curves were created of the derived K^{trans} , k_{ep} , v_e and v_p parameters to check for correlations with histologic grade, which was 0 for the low-risk grades and 1 for the high-risk grades. The curves show no correlation with the histologic grade for all four model parameters (Figure 4.12 in section 4.3). The frequencies of the low-risk and high-risk histologic tumor grades were tested with a chi-square test. The test indicates that there is evidence to reject the null hypothesis which states that the histologic subtypes have frequencies given by splitting the K^{trans} values by the median value. This means that there is statistical evidence to indicate that there is no correlation between derived K^{trans} values and histological grade based on the results in this project.

Even though no correlation was observed between the derived model parameters and histologic grade in this project, Ye et al. did find a correlation between parameters derived from ETM and low- and high-risk histologic subtype [13]. Ye et al. found higher K^{trans} , k_{ep} , V_e and V_p for the low-risk histologic type than for the high-risk type. Ye et al. analyzed for correlations with low- and high-risk types, whereas the correlation analysis carried out in this project looks at histologic grade. In this project, low-risk grade

includes endometrial carcinomas diagnosed as endometrioid of grades 1 or 2, while high-risk grades include the non-endometrioid type and the endometrioid type of grade 3. Ye et al. classified patients with grade 1 and 2 endometrioid adenocarcinoma as the low-risk types, whereas the patients with endometrioid grade 3 and non-endometrioid were classified as the high-risk disease type [13]. Hence, there might be a basis for comparison between the findings by Ye et al. and the findings in the present study. Halvorsen et al. calculated perfusion parameters for the endometrioid histologic type and the non-endometrioid histologic type, and found no significant differences between the perfusion parameters for the different tumor grades [1]. The differences in the findings between the studies highlight the need for further research in the field to ascertain whether these observations are coincidental or if a correlation is present between the derived perfusion parameters and histologic type and grade.

5.3 Future work

The AIF seems to influence the model parameters derived from ETM a lot. Great differences were observed between the mean parameters from ETM when three different methods were used for estimating the AIF. This is one part of the research field that might benefit from further research. A precise and time-efficient standardized approach for finding the concentration of CA in a feeding artery is needed. An automatic algorithm for estimating the AIF is time efficient, but research is necessary in order to implement an algorithm that also is precise.

Developing a method for automatically finding an AIF for endometrial cancer data could enlighten the work when implementing quantitative models that require an input plasma concentration. An automatic algorithm for finding the AIF could be created by further developing the algorithm presented by Tønnes et al [26]. Machine learning and deep learning methods might also be relevant for developing a robust algorithm for estimating the AIF for endometrial cancer data. Automatic algorithms using deep learning have been developed for brain data like for instance the one proposed by Fan et al [55].

It would also be interesting to test commercially available software, like for instance the nordicICE software (Nordic-NeuroLab AS, Bergen, Norway) on the same data as we have analyzed in this project. Subsequently, a comparison can be carried out between

the population-based AIF developed within this project and the population-based AIF suggested by the software. It would also be interesting to see if the results obtained from ETM using commercial software are in line with the results obtained in this project when using the same tumor masks and analyzing the same patient data as in the present project.

In this project, no methods were implemented to facilitate the conversion from MRI signal to real CA concentration. The MRI signal intensity was solely subtracted by the baseline signal intensity as suggested by Hanson et al [52]. In the future, it could be relevant to implement different methods for converting from MRI signal to CA concentration in order to see how this affects the derived model parameters for endometrial cancer data.

Implementing a way of handling motion could also be relevant for endometrial cancer data. A great deal of research and software evolves around brain imaging data. Other organs in the body have bigger variations in anatomy between patients and some organs move more than others. In addition, some organs are more sensitive to patient movement. For this reason, software tailored to brain imaging data might not suit other organs as well. For endometrial cancer data, we need to handle the fact that the anatomy of the pelvis varies between patients and that the DCE-MRI images might be affected by motion. Developing robust ways of handling these issues might be important in future research.

Chapter 6

Conclusions

In this thesis, we found that modeling based on the average signal intensity inside the tumor exhibits higher consistency in the derived perfusion parameters than modeling based on the voxelwise signal intensity. Some of the model parameters derived from ETM when modeling based on the voxelwise signal intensity exhibit higher levels of outliers.

Different methods for estimating the arterial input function were successfully implemented in Python and tested on data from 20 patients. It was observed that the AIF affects the parameters derived from ETM quite a lot and might be a main reason for the deviations in the model parameters derived from ETM. The findings in this thesis indicate that the population-based AIF method is the most robust method for estimating the AIF.

The model parameters derived in this project are mostly higher than the parameters derived in three other studies that were chosen as a basis for comparison [1][12][13]. The K^{trans} parameters derived in this project exhibit the highest similarity to the parameters derived by Ye et al. [13]. The k_{ep} values derived in this project are slightly more similar to the k_{ep} values derived in the three studies [1][12][13].

In this project, no correlation was observed between the calculated perfusion parameters and low-risk and high-risk histologic tumor grades.

Source code

The Python code used in this thesis is available in the Github repository "DCE-MRI-analysis-endometrial-cancer".

Most of the algorithms used for running the extended Tofts' method (ETM) on DCE-MRI data from patients with endometrial cancer are included in this repository. Two DICOM images are required for running ETM, including the whole-volume tumor mask and the DCE-MRI image. In addition, an arterial input function (AIF) is required. Scripts illustrating how the AIF was estimated are also included in the repository. Examples of how the resulting parameters were analyzed and visualized can also be found in the Github repository.

Link to the Github repository:

<https://github.com/ingridaase/DCE-MRI-analysis-endometrial-cancer>

Contents of the repository

The GitHub repository is organized into three folders:

The arterial input function: This folder contains three different methods for estimating the AIF, including manual annotation of the AIF, an automatic algorithm for estimating the AIF and a population-based AIF. The population-based AIF is based on manually annotated AIFs, whereas the two other methodologies require an input DCE-MRI image in DICOM format.

Extended Tofts method: Scripts and functions used for running ETM are included in this folder. An arterial input function is required for ETM. This folder contains scripts for running ETM inside the research information system, in addition to scripts for running ETM on a local machine.

Visualization and statistics: This folder contains examples of how the resulting model parameters were analyzed and visualized. Additionally, clinical parameters were imported and included in the analysis.

Requirements

The requirements for the algorithms in this project are included in an "environment.yml" file, which can be found in the repository.

Appendix A

Extended Tofts' model

This appendix includes model parameters obtained from numerical modeling with extended Tofts' method (ETM) in addition to results from statistical analysis and an mathematical derivation of extended Tofts' method.

A.1 Analytical solution to ETM

Equation (A.1) shows the leakage across the endothelium, which is thought to be proportional to the difference between the concentration in the plasma (C_p) and the concentration in the EES (C_e .)

$$v_e \frac{dC_e(t)}{dt} = K^{trans}(C_p(t) - C_e(t)) \quad (\text{A.1})$$

Equation (A.1) is rewritten by dividing both sides of the equation by v_e giving the expression in equation (A.2).

$$\frac{dC_e(t)}{dt} = \frac{K^{trans}}{v_e}(C_p(t) - C_e(t)) \quad (\text{A.2})$$

The coherence $k_{ep} = \frac{K^{trans}}{v_e}$ is used giving the expression in equation A.3

$$\frac{dC_e(t)}{dt} = k_{ep}C_p(t) - k_{ep}C_e(t) \quad (\text{A.3})$$

All terms in equation (A.3) are multiplied with the integrating factor ($e^{k_{ep}t}$) giving the expression in equation A.4.

$$\frac{dC_e(t)}{dt} e^{k_{ep}t} = k_{ep}C_p(t)e^{k_{ep}t} - k_{ep}C_e(t)e^{k_{ep}t} \quad (\text{A.4})$$

The expression is then rewritten giving equation (A.5).

$$\frac{dC_e(t)}{dt} e^{k_{ep}t} + k_{ep}C_e(t)e^{k_{ep}t} = k_{ep}C_p(t)e^{k_{ep}t} \quad (\text{A.5})$$

The product rule and chain rule for derivation is used backwards in order to find the expression in equation (A.6).

$$[C_e(t)e^{k_{ep}t}]' = k_{ep}C_p(t)e^{k_{ep}t} \quad (\text{A.6})$$

Both sides of the expression in equation (A.6) is integrated as shown in equation (A.7) and (A.8). The expression is integrated over the total time t and τ is introduced as the differential of t .

$$\int [C_e(t)e^{k_{ep}t}]' = \int_0^t k_{ep}C_p(\tau)e^{k_{ep}\tau} d\tau \quad (\text{A.7})$$

$$C_e(t)e^{k_{ep}t} = k_{ep} \int_0^t C_p(\tau)e^{k_{ep}\tau} d\tau \quad (\text{A.8})$$

Both sides of the equation are multiplied with v_e , as shown in equation (A.9).

$$C_e(t)v_e = k_{ep}v_e e^{-k_{ep}t} \int_0^t C_p(\tau)e^{k_{ep}\tau} d\tau \quad (\text{A.9})$$

The fact that the total tissue concentration is the sum of the plasma concentration and the EES concentration ($C_t = C_e v_e + C_p v_e$) is utilized to find the total tissue concentration.

$$C_t(t) - C_p(t)v_p = K^{trans} e^{-k_{ep}t} \int_0^t C_p(\tau)e^{k_{ep}\tau} d\tau \quad (\text{A.10})$$

The expression in equation (A.10) is rewritten to get the total tissue concentration alone on one side of the equation as shown in equation (A.11).

$$C_t(t) = C_p(t)v_p + K^{trans} e^{-k_{ep}t} \int_0^t C_p(\tau)e^{k_{ep}\tau} d\tau \quad (\text{A.11})$$

Extended Tofts' model is then shown in equation (A.12).

$$C_t(t) = C_p(t)v_p + K^{trans} \int_0^t C_p(\tau)e^{-k_{ep}(t-\tau)} d\tau \quad (\text{A.12})$$

A.2 Model parameters obtained from ETM

A.2.1 Manual AIF

Average modeling

Table A.1: Model parameters from extended Tofts' method when using manually annotated arterial input functions and modeling based on the average signal intensity inside the tumor ($n=20$).

K^{trans}	k_{ep}	v_e	v_p
0.15423085479536805	0.6567658423065185	0.23483385532615308	0.11095160272871749
0.10372078764608236	0.31900860611546605	0.32513476331901947	0.171742042077636
0.1631953189425114	0.7330931247658379	0.22261198943127272	0.2365301224891942
0.41303666075351897	1.5938313205519217	0.25914703483834794	0.330509445992213
0.22156083752010053	1.9044244332271476	0.11634005196239475	0.20726377113820382
0.2362367126598966	1.9743097415245023	0.11965534469656304	0.21721130753175777
0.11535929235627276	1.4169487081621335	0.0814138801861788	0.08309369565863062
0.1691788343497397	0.8181715835304777	0.20677671744564768	0.2095263596310395
0.046563269439565375	0.04656326943956549	0.9999999999999974	0.24022707528742365
0.29003330346019274	0.6226684073978682	0.4657909410760731	0.2428095759472152
0.2769394273717008	1.6871034652632786	0.16415082600075354	0.2155692459883353
0.1244535745239698	0.46020093592130973	0.2704331191217965	0.08849465141421096
0.17292825812328777	0.3187084848355316	0.5425906944790841	0.12226476037143853
0.1105860685927547	0.3085834932400735	0.3583667662570672	0.10243777567400988
0.10155294642335906	0.537473105445677	0.18894516840828818	0.07399486031467323
0.09525026424624458	0.24096124159901333	0.39529288450775735	0.22831109591866122
0.09485679833227781	0.22834448504598442	0.4154109450603783	0.32595054055352585
0.13899099057432857	0.4755086754932617	0.2922995893400859	0.11423799912688808
0.09087815867251099	0.9447978255426718	0.09618794224077783	0.10943988652185875
0.07989819279110441	0.26196642755851357	0.30499401597274567	0.2041674027506683

Voxelwise modeling

Table A.2: Model parameters from extended Tofts' method when using manually annotated arterial input functions and modeling based on the voxelwise signal intensity inside the tumor ($n=20$).

K^{trans}	k_{ep}	v_e	v_p
0.16660405084254393	0.7374365302227506	0.24213088528897966	0.10924924702306471
0.1122813836690585	0.38144260338696595	0.349450256051366	0.1691733032087281
0.16434411394080067	0.6505638736100757	0.34775887113138226	0.24428145618205765
0.4046612639442145	1.522202696178149	0.2740212009977999	0.32958872757419505
0.1432980784521802	1.2754208341374311	0.1935865627700347	0.22864063580570498
0.18667702383335288	1.4797492391096796	0.12325764338402503	0.23163268338258422
0.0966702344505107	1.2559909253350021	0.08994945998762288	0.08902085276786882
0.18242085089598134	0.7332044921932774	0.24482230728730842	0.20779114424647593
0.08693601561839058	0.3196351868101804	0.7334756792823728	0.21994411493416213
0.31476172085956255	0.689874855319853	0.5119157081300165	0.24034967036949903
0.2570529149942951	1.641926686555167	0.16914598771202174	0.21979800427437163
0.1332971154099629	0.4839601599737208	0.2929328503625259	0.08670206580519374
0.18189752419685049	0.3646052224169786	0.5702078567506801	0.12041713276092914
0.1245570905758882	0.3940936035765084	0.4540378800228382	0.10092626419073718
0.10775451856435032	0.7237982846230039	0.23102697918620835	0.07326252406052246
0.09820266563100505	0.2662509047994742	0.43108328443801913	0.22714450740956246
0.11423721662691266	0.33616965779704333	0.5560723275693455	0.3195583259599061
0.14573988887061015	0.5090383644100017	0.3072862536070443	0.11306209307398887
0.09677853697852801	1.0696913298025514	0.10691611585710228	0.10978221880500208
0.08705240236753971	0.27415597148435455	0.4085917294651154	0.20242514182912938

A.2.2 Population-based AIF

Average modeling

Table A.3: Model parameters derived from extended Tofts' method when using a population-based arterial input function and modeling based on the average signal intensity inside the tumor ($n=20$).

K^{trans}	k_{ep}	v_e	v_p
0.15813737505805814	0.4528053998749944	0.34923915461634286	0.19321175534895763
0.09641047902777591	0.31622978429516196	0.30487475821628646	0.22188147550412682
0.08491730739712691	0.3686803730729418	0.23032771364893456	0.22400403582214107
0.2397728271295572	0.8994800441950082	0.2665682564910514	0.2339038153016921
0.0984444971070331	1.9669662234571743	0.0500489006537211	0.23449630490864953
0.1625086435452934	1.5096322719128306	0.10764783356107069	0.17521371308773642
0.09696891778404279	0.9706342815781749	0.09990263029488199	0.08688522331171378
0.09708765922979741	0.443447563938478	0.2189383077618325	0.16698087734275852
0.08812941850037874	0.08812941850045812	0.9999999999990993	0.3747010483156715
0.19431315507294183	0.5526251669425487	0.35161836032187577	0.2753014668636027
0.2287943717987728	1.7213038316136158	0.13291922529696124	0.24833401975150923
0.13034656155049187	0.37368241214626285	0.34881642087953824	0.09068020507052035
0.10571034085503103	0.2717624608964724	0.3889806579846261	0.06449801603630007
0.09513856269598212	0.2473331144357029	0.3846576020078964	0.11106566118993817
0.0797892260085647	0.3529983803701252	0.22603283880482467	0.06887519965182552
0.11495048696864728	0.4271994411896853	0.2690792072398964	0.2693134040407569
0.05898609846566856	0.42963507647749405	0.1372934885793909	0.2629428795651916
0.11595224696663478	0.37497992529580415	0.309222545380704	0.099083575835257
0.042126697789076836	0.42478748617607187	0.09917123069773193	0.18255029770683354
0.16191284968974015	0.7532573109439428	0.21495025317024724	0.26820553851652085

Voxelwise modeling

Table A.4: Table showing all the optimized parameters from extended Tofts' method when using a population-based arterial input function and modeling based on the voxelwise signal intensity inside the tumor ($n=20$).

K^{trans}	k_{ep}	v_e	v_p
0.1774159215827685	0.5591310665706384	0.34370685137535395	0.19162286827137695
0.11160675903704076	0.46668892754611024	0.3094343063461616	0.2210757497367626
0.1109686490706205	0.6696212432988746	0.35421183025959846	0.22317218353713758
0.2739984473891227	1.0558819674281257	0.26972657489651414	0.23353565037214763
0.04675852139093551	2.0650124796711506	0.2770204734603566	0.25112237644220137
0.14573319473766108	1.3739182141916713	0.10901793470656752	0.18437693519368056
0.10118738252753534	1.430759690653251	0.10968807384156531	0.09000382619194326
0.11086012962315736	0.4583361686383868	0.24858642522921248	0.16638715259733078
0.13692916711268313	0.295358063027237	0.8350080233415342	0.36015799634741125
0.218617959669452	0.6590516116803323	0.38927645231152586	0.2753172215598418
0.18178336425896993	1.320742523765689	0.12384721091907197	0.2671456102700211
0.14046508383631764	0.4109558646570405	0.3608813438828635	0.08998424535862498
0.1118769318571233	0.31676398972658604	0.39877444524698674	0.06440097973178953
0.10843260776291581	0.35094982082589016	0.46264178535246525	0.11042138268795013
0.08662442500944419	1.7752100251817515	0.28927102283456796	0.06913009148125461
0.14810525639237954	0.7892243202000859	0.2825282125641038	0.26535136268576903
0.0815600860618996	0.6138506172746724	0.3347538935290195	0.26194445903152386
0.12299172835900994	0.4188678060063562	0.3127905265861073	0.0994889375779011
0.05531552749408951	0.6475600392495335	0.1880008453544567	0.18266358009051387
0.20169537091034964	1.1057701070039054	0.21510449971649823	0.2652860487435429

Erosion of tumor masks (average modeling)

Table A.5: Model parameters derived from extended Tofts' method when using a population-based arterial input function and an eroded tumor mask ($n=20$). Modeling was performed based on the average signal intensity inside the tumor.

K^{trans}	k_{ep}	v_e	v_p
0.15635105453869336	0.46883053285352627	0.33349162134783816	0.19933761076435777
0.08730204917918324	0.34774009157617103	0.2510554615186213	0.20854019114110442
0.08875906369016982	0.4288737180473158	0.2069585053947685	0.23024141156574524
0.2449265175658345	0.9693691813863602	0.25266588031563847	0.22708643749527693
0.10796088287210705	2.450442946755979	0.044057701084218734	0.2316543193512844
0.16443504323565142	1.8003606985984975	0.09133449944983633	0.1678116957908322
0.10531885729814927	1.399734639128608	0.07524201684664641	0.08315421057577102
0.09323884532136502	0.512062341118515	0.18208494910541612	0.15592520999465762
0.10192865772642562	0.10192865772642572	0.9999999999999991	0.3561541206125725
0.19116405452805402	0.615983197031474	0.31033972265689314	0.25093308643476725
0.22288765745888242	2.04411164560418	0.10903888637305977	0.24285719665511887
0.1575288852503131	0.46439060184076425	0.3392163506881831	0.14845875624401159
0.1136827030633013	0.2844796326464683	0.3996163170126782	0.06725185755490354
0.09493667767232765	0.25941237017916075	0.36596819807305453	0.10951160697204827
0.06588181169697763	0.3509241479537254	0.1877380399187152	0.0683336539235425
0.12098061952599809	0.496356501538908	0.24373735238867372	0.28058156109349686
0.043052412840854835	0.6402957778769548	0.06723832067674228	0.2511374712167736
0.11507200878462011	0.4196345376860078	0.27421958502072324	0.10359625569107725
0.045931728843318725	0.5810266233627639	0.0790527094567253	0.1738708211013675
0.1707749777093008	1.1323708963265602	0.15081187468107768	0.2517586471409868

Dilation of tumor masks (average modeling)

Table A.6: Model parameters derived from extended Tofts' method when using a population-based arterial input function and a dilated tumor mask ($n=20$). Modeling was based on the average signal intensity inside the tumor.

K^{trans}	k_{ep}	v_e	v_p
0.18493149970179715	0.500558502998212	0.36945032117945603	0.20160530948876895
0.1136513165741379	0.34189949150250876	0.332411481733087	0.23270293480284254
0.09241273259178352	0.4259824870023618	0.21694021564616847	0.21997121348563858
0.27510056760129314	0.9810282663013938	0.2804206331775318	0.24656610575787163
0.11425282080999316	2.0333056361223543	0.056190677279526306	0.23771623907458964
0.18113913044350868	1.5319656542949125	0.11823968111535635	0.18580104514537532
0.10673207373755147	0.8490828019120252	0.12570278599119494	0.09507562950120588
0.10769778535324	0.4873637397609781	0.22098029985993442	0.17441613608330606
0.07893152765381199	0.078931527653812	0.9999999999999999	0.40740000577047236
0.21558076886022962	0.6366583796258973	0.33861294496258043	0.28447595092012595
0.26156429292251393	1.6794094901655028	0.15574777590231267	0.263619487512572
0.13529167631737457	0.39829349773730977	0.3396783454562062	0.08486328901878211
0.10299704515284576	0.2849219959711289	0.3614920806720814	0.06519817173746954
0.10094386119669883	0.2687831574302832	0.37555872980203975	0.11263542629647633
0.09695375762701818	0.3847249069542088	0.25200800851336075	0.07392261961581359
0.12537627509974075	0.49128675369597596	0.25519978740832816	0.26773316585908513
0.08847770997765302	0.5526470738065145	0.1600980339373509	0.27101564711773896
0.1266802285121551	0.41029106669652216	0.3087569747304686	0.10297035183185328
0.05166591018756534	0.5338149419640918	0.09678618211297793	0.18987744265957174
0.21052417053539174	0.8040301233867461	0.26183617306354035	0.28452842661821565

A.2.3 Semi-automatic AIF

2% bright voxels - average modeling

Table A.7: Model parameters derived from extended Tofts' method when using a semi-automatic arterial input function, choosing 2% bright voxels and modeling based on the average signal intensity inside the tumor ($n=13$).

K^{trans}	k_{ep}	v_e	v_p
1.4383972598195145	2.075340042939111	0.6930899178249585	0.0524922444893312
1.0385744470992628	2.0254766642473143	0.5127555727654886	0.24727797965618023
0.16591391246169973	0.771887358254332	0.21494575690023432	0.3426389546691018
-0.00017450522316470293	-0.6955751763398094	0.0002508790265963314	0.37079574917310254
-0.02213909569795426	-0.022139095698057217	0.999999999953496	0.5111971177923046
0.1417127094589002	0.7873115843471091	0.17999571234102665	0.3938697979367327
0.5350823734235554	5.360982207160625	0.09981051097480788	0.7839881781608253
0.06646240643615803	0.5448173720807084	0.12199024818597817	0.46102259145305974
0.31713280347662787	0.6506577146341268	0.48740343247133516	0.2099799299718968
0.11091097071726841	0.7663681202792066	0.14472283982384448	0.40801362353905757
2.8659399572701507	2.865939957845991	0.9999999997990745	0.406261724097611
0.11606781040825165	1.079342779962389	0.10753563424243795	0.15515398554778043
-0.0008476910728239226	-0.7010788740489958	0.0012091236866519537	0.45258661135013434

2% bright voxels - voxelwise modeling

Table A.8: Model parameters derived from extended Tofts' method when using a semi-automatic arterial input function, choosing 2% bright voxels and modeling based on the voxelwise signal intensity inside the tumor ($n=13$).

K^{trans}	k_{ep}	v_e	v_p
1.4396398413382239	2.0651353170224858	0.6943533440530534	0.05659262386998301
0.9291712426127208	1.8923113735345438	0.4975904563115487	0.2925419414313641
0.159097787578042	0.5568274165491081	0.3887290116685824	0.3524458704155444
0.07831693907874226	0.602051149450451	0.220837952801527	0.3269252704203262
-0.016961694596049848	0.0029974257680456663	0.760579635017835	0.5065256703473364
0.16013112055451906	4.338485674143834	0.24203697828509674	0.3884183566536897
0.4518676046897229	4.999155067127976	0.32430286377706075	0.8315671564449407
0.11349258288292172	17.541227962685973	0.24052658169123645	0.42028388315105547
0.32908379183338016	0.6825527253755697	0.5132417540453543	0.21093073565460593
0.1238030786216983	3.476400122709239	0.19831927360657192	0.41102668277445864
2.8491033593447863	2.8996631907830954	0.9801213453374892	0.416333691698925
0.11194011087778732	1.0568372973598728	0.12019711873768392	0.1583933034420035
0.09025126304744029	-0.22215336132024932	0.06434742686314421	0.39445017181320885

3% bright voxels - average modeling

Table A.9: Model parameters from extended Tofts' method when using a semi-automatic arterial input function, choosing 3% bright voxels and modeling based on the average signal intensity inside the tumor ($n=18$).

K^{trans}	k_{ep}	v_e	v_p
0.7969590622399121	0.7969590622399122	0.9999999999999999	0.207407797580898
0.14302603230328395	0.3749545635392854	0.3814489706518762	0.34459330006089217
-0.004167963146542596	-0.14002441075113303	0.02976597526234454	0.6162817197328934
-0.000236881534262391	-0.6546600941600806	0.0003618389701396212	0.3787659519310713
-0.017960312883476704	-0.017960312883477568	0.9999999999999518	0.5226639150036466
0.03997670792449439	0.8828931526813114	0.04527921391516823	0.40040049466016403
0.060299938747684766	0.06029993874768483	0.9999999999999989	0.6309963887890916
0.6719977875516491	0.8911599692342147	0.7540708859814536	$1.0601154047435955 \times 10^{-9}$
-0.03545237454697829	-0.035452374546984466	0.9999999999998259	0.5535534048162044
0.0987901571335116	0.6042686797055045	0.16348713817445878	0.432294099594772
0.3455604942891316	0.6155063115556556	0.5614247779454089	0.24274323315243526
0.05614919925710979	0.28219085039328995	0.19897597380940787	0.2819010998214092
0.18157765729235392	0.8039231977070124	0.2258644330829839	0.2466141013079857
0.13329500980041425	1.3489141357715106	0.09881652676445284	0.4282292563338913
-0.011676357355517626	-0.011676357356837195	0.99999999886988	0.5169170691211397
1.0800037597754488	1.2042628230960633	0.8968173218192069	0.368129694489481
0.11997692984897382	1.1083694869339662	0.10824633054529563	0.16533993096934718
1.5915628465275737	2.243808675251222	0.709313081851499	0.06664800343840657

3% bright voxels - voxelwise modeling

Table A.10: Model parameters derived from extended Tofts' model when using a semi-automatic arterial input function, choosing 3% bright voxels and modeling based on the voxelwise signal intensity inside the tumor ($n=18$).

K^{trans}	k_{ep}	v_e	v_p
0.7559574439239323	0.7687328037264526	0.9742859608931053	0.23571907255338945
0.16681752191173632	0.5382184082631727	0.4198668481087619	0.3390544929239424
0.06039914558290123	95.44629335820234	0.6128147650294609	0.5573082037041228
0.07593302386030172	0.8773661616189299	0.22847761201869282	0.33689562381061844
-0.009643576832283124	0.046057003668151485	0.7283511294808849	0.5163229812717167
0.055300669364134414	40.176522480887925	0.2122823896342765	0.3802124420906021
0.14189214800486782	0.6505485746261126	0.8000406811948391	0.5931394963240938
0.44406931444435244	0.05393859961501542	0.46270069124975477	0.42992888127393186
-0.033346853786853745	-0.0533889816558951	0.9088914376520847	0.5506952022553319
0.14106596492441648	14.967462514390057	0.24818197256703592	0.40205516182528833
0.3609562806721745	0.662748066315397	0.5892130885554121	0.24345696066408984
0.0626564644459377	5.72981643487707	0.43856168997513983	0.27768123763869257
0.17367788381556654	0.6479485432135654	0.437331320720171	0.2510064675972397
0.09943154478421148	1.556243398423381	0.24726240655013448	0.43868393026347763
0.0027183851437656663	0.20610074423455085	0.68035611028331	0.5052151481285861
1.071046150207796	1.2590044264996463	0.8683714869693313	0.3974744785858602
0.11327637754789825	1.5681105964919344	0.12216690913193413	0.1693557856342006
1.5886534903206053	2.2829634926920885	0.7002458640604474	0.07441297206479068

Results from the research information system - average modeling

Table A.11: Model parameters derived from extended Tofts' model when using a population-based arterial input function ($n=60$).

K^{trans}	k_{ep}	v_e	v_p
0.16542327	0.49676086	0.33300384	0.194340235
0.23256041	0.9904803	0.2347956	0.194580104
0.27037226	0.57345212	0.47148184	0.202776717
0.20624328	0.58602376	0.35193672	0.183879462
0.15178383	0.69775867	0.21753055	0.158912821
0.29308355	0.91866561	0.3190318	0.238503412
0.16303877	0.54018338	0.30182114	0.273227942
0.09986648	0.35269868	0.28314958	0.223914315
0.33128052	0.53127226	0.62356073	0.270940896
0.03342967	0.21493156	0.15553634	0.00892526172
0.09010848	0.42511352	0.21196334	0.225195469
0.17295343	0.73261636	0.2360764	0.118410670e
0.17692048	0.45829554	0.38604015	0.152446344
0.23056603	0.33682006	0.68453771	0.203846522
0.1249623	0.45267244	0.27605457	0.272180669
0.24044423	0.92003105	0.26134361	0.350970003
0.17961642	0.44223934	0.40615207	0.143373767
0.02579387	0.02579387	1.	1.15458493e-13
0.311868	0.66438518	0.46940843	0.351546986
0.92280809	3.17347154	0.29078821	3.27044394e-18
0.08361726	0.37761211	0.22143691	0.114788485
0.29042636	0.73126807	0.39715444	0.321594346
0.19004271	0.54916977	0.34605456	0.251709521
0.28156558	1.0477028	0.26874566	0.248503750
0.21555801	1.41680835	0.15214338	0.461792334
0.1550721	0.29417766	0.52713757	0.0844053852
0.0661958	0.34126671	0.19397086	.0269223504
0.17093493	0.45069361	0.3792708	0.293268464
0.11169726	2.33845405	0.04776543	0.234305393
0.18844094	0.71252316	0.26446992	0.222376194
0.08861045	0.28386144	0.31216093	0.0516803768
0.20561063	0.53505781	0.38427741	0.307067151
0.17248314	1.66050855	0.10387368	0.176295353
0.13833153	0.78103561	0.17711297	0.153348389
0.10490463	1.09407939	0.09588393	0.0875709439
0.17406573	0.76650181	0.22709109	0.235798746
0.12967012	0.47104598	0.27528124	0.109230396
0.15294128	0.48182379	0.3174216	0.169935850
0.14706566	0.71655008	0.20524128	0.140828107
0.10219078	0.49533215	0.20630758	0.168016606
0.08371963	0.08371963	1.	0.383662524
0.37027374	0.41129405	0.90026526	0.322582524
0.19573294	0.93166178	0.21009012	0.440219670
0.15806792	0.97094108	0.16279868	0.182857589
0.14971518	0.33826724	0.44259437	0.166306497
0.23885802	1.86411787	0.12813461	0.250263176
0.12661061	0.15327932	0.82601236	0.137524454
0.24436547	1.48101994	0.1649981	0.240637796
0.10775548	0.28721322	0.37517589	0.0652509920
0.09736602	0.26623017	0.36572121	0.111866275
0.08190963	0.3779122	0.21674248	0.0698179834
0.18590538	0.35065234	0.53017009	0.191066203
0.13662173	0.48200584	0.28344415	0.226748315
0.06408755	0.19904857	0.32196942	0.0557061951
0.12311678	0.49322236	0.2496172	0.270300242
0.07170706	0.55516535	0.12916343	0.118324969
0.06763336	0.56207565	0.12032786	0.263569165
0.26061144	0.47889961	0.54418804	0.544838378
0.04825089	0.55199215	0.08741227	0.182713485
0.18714453	0.92359505	0.20262617	0.266795511

Results from the research information system - voxelwise modeling

Table A.12: Model parameters derived from extended Tofts' method when using a population-based arterial input function (n=60).

K^{trans}	k_{ep}	v_e	v_p
0.17741594	0.55913112	0.34370685	0.191622865
0.24247789	1.09811571	0.24616276	0.193407256
0.31913579	0.7347059	0.49583903	0.195380776
0.23181264	0.70117384	0.36431619	0.179030870
0.16811924	0.75711531	0.24977231	0.156259520
0.29281511	0.93319312	0.32362244	0.238830222
0.16914205	0.57402425	0.30491274	0.272073850
0.11160677	0.46668933	0.3094343	0.221075744
0.35278831	0.60390602	0.66766428	0.268874962
0.03384891	0.19129863	0.36452851	0.0111545843
0.11096835	0.66965041	0.3541889	0.223172382
0.18815981	0.87577072	0.246242	0.115745292
0.20579457	0.66014328	0.40973213	0.151821694
0.25128839	0.40822826	0.70459243	0.200411470
0.13757558	0.54714243	0.3765389	0.270261981
0.2553927	1.12118318	0.27109477	0.349383608
0.19620117	0.55535438	0.42860012	0.139395196
0.03001815	0.20100709	0.77922388	0.00575648065
0.33614032	0.82530329	0.49744151	0.348991145
0.97076173	3.3930968	0.29453558	0.000491226485
0.1019642	0.48809066	0.31876801	0.111109243
0.31369414	0.86060419	0.4084257	0.317786030
0.20312886	0.63640156	0.38994914	0.250185887
0.2932383	1.0617965	0.28202689	0.247068225
0.19517219	1.62212433	0.19439257	0.462235263
0.15552707	0.29210254	0.53825213	0.0858375646
0.07967333	1.91931466	0.29022351	0.265833261
0.18440338	0.50157937	0.39386663	0.290319538
0.04674222	1.68280063	0.27701787	0.251129678
0.20744153	0.85356552	0.27285025	0.219525663
0.09003619	0.24194955	0.43949403	0.0548463135
0.24533601	1.9340657	0.41504335	0.300620284
0.14573354	1.37391631	0.10901808	0.184376751
0.17298172	0.85423206	0.29480426	0.149544270
0.10119601	1.67345845	0.10970926	0.0900151761
0.17966728	0.82469447	0.23399428	0.235147042
0.14516403	0.6541712	0.28643951	0.105904291
0.1547536	0.48689754	0.32609132	0.169924696
0.17060925	1.042073	0.2225611	0.137480431
0.11086018	0.45833647	0.24858642	0.166387136
0.13692907	0.29535543	0.83500812	0.360158093
0.39279109	0.50460052	0.85443651	0.338536689
0.23128393	1.1963243	0.25820921	0.434341135
0.15533695	0.96278629	0.22638687	0.186678102
0.16122452	0.35980284	0.48527186	0.164646352
0.18187948	1.32084593	0.12386719	0.267116691
0.14432216	0.20865441	0.82020925	0.128006546
0.24096622	1.54832601	0.17533563	0.241436526
0.11187692	0.31676601	0.39877442	0.0644009856
0.10843262	0.35094856	0.46264178	0.110421291
0.08662398	1.77187296	0.28924703	0.0691303650
0.19603965	0.40043602	0.55469546	0.188795235
0.14927703	0.5145374	0.36374376	0.230271979
0.07608396	0.23292227	0.58678887	0.0502156731
0.1481051	0.79096671	0.28252815	0.265351551
0.08803375	0.76208467	0.16930632	0.115829689
0.08156005	0.61305831	0.33431394	0.261944258
0.31602702	0.84277893	0.57843631	0.536277809
0.05531562	0.64754813	0.18800604	0.182663657
0.20169528	1.10577114	0.21510447	0.265286087

A.3 Statistical evaluation

A.3.1 Spearman's rank correlation coefficient

Table A.13: Spearman correlation coefficients and p-values for all of the AIF methodologies when comparing average and voxelwise modeling results. The bottom row shows the correlation coefficient obtained from modeling in the research environment, while the rest of the coefficients were obtained from the local modeling environment.

	Correlation coefficient	p-value
Manual AIF (n=20)	0.934	1.81×10^{-9}
Population-based AIF (n=20)	0.849	2.13×10^{-6}
Automatic AIF (2% brightest voxels, n=13)	0.973	2.62×10^{-8}
Automatic AIF (3% brightest voxels, n=18)	0.969	3.85×10^{-11}
Population-based AIF (n=63)	0.972	3.60×10^{-40}

Table A.14: Spearman correlation coefficients and p-values for the derived K^{trans} values from the three different methods for estimating the AIF.

	Correlation coefficient	p-value
Population-based vs. manual AIF (n=20)	0.645	0.002
Automatic vs. manual AIF (n=18)	-0.253	0.311
Automatic vs. population-based AIF (n=18)	0.178	0.478

A.3.2 Wilcoxon signed-rank test

Table A.15: p-values for the derived K^{trans} values from modeling based on the average signal intensity and from modeling based in the voxelwise signal intensity. The bottom row shows the p-value for the model parameters obtained from the research environment, while the rest of the values are based on results from the local modeling environment. Only the population-based method exhibits similar median values from modeling based on the average signal intensity and modeling based on the voxelwise signal intensity.

	p-value
Manual AIF (n=20)	0.294
Semi-automatic AIF (2%, n=13)	0.588
Semi-automatic AIF (2%, n=18)	0.304
Population-based AIF (n=20)	0.0327
Population-based AIF (n=63)	1.63×10^{-7}

Table A.16: p -values for the derived K^{trans} values from the three different methods for estimating the AIF when testing the null hypothesis by the Wilcoxon signed-rank test.

	p-value
Population-based vs. manual AIF (n=20)	0.0083
Automatic vs. manual AIF (n=18)	0.6397
Automatic vs. population-based AIF (n=18)	0.4423

Appendix B

The arterial input function

B.1 Cost values from the semi-automatic AIF

Table B.1: Cost values for different percentages of bright voxels, 2% and 3% bright voxels. The cost values are based on how well a Parker AIF fits the derived derived AIF from the semi-automatic algorithm. In this table "-" illustrates that the algorithm did not find an AIF for this patient.

Patient	2%	3%
1	2.0067	1.4996
2	0.6190	0.0669
3	0.0724	0.0803
4	-	-
5	0.0279	0.0279
6	0.0966	0.0762
7	-	-
8	0.1497	0.0231
9	-	0.0845
10	-	0.1132
11	0.4398	0.0622
12	0.0793	0.0562
13	0.8010	0.8102
14	-	0.0398
15	-	0.0921
16	0.2714	0.0963
17	1.5414	0.0441
18	-	1.3340
19	0.0546	0.0551
20	0.3541	0.6410

Bibliography

- [1] Ingrid S. Haldorsen et al. “Dynamic contrast-enhanced MRI in endometrial carcinoma identifies patients at increased risk of recurrence”. In: *European Radiology* 23 (10 Oct. 2013), pp. 2916–2925. ISSN: 09387994. DOI: 10.1007/s00330-013-2901-3.
- [2] Kreftforeningen. *Livmorkreft*. URL: <https://www.helsenorge.no/sykdom/kreft/livmorkreft/>. (accessed: 29.11.2022).
- [3] Kelly Passarello, Shiney Kurian, and Valerie Villanueva. “Endometrial Cancer: An Overview of Pathophysiology, Management, and Care”. In: *Seminars in Oncology Nursing* 35.2 (2019). Gynecology Oncology, pp. 157–165. ISSN: 0749-2081. DOI: <https://doi.org/10.1016/j.soncn.2019.02.002>.
- [4] American Cancer Society. *What is Endometrial Cancer?* URL: <https://www.cancer.org/cancer/endometrial-cancer/about/what-is-endometrial-cancer.html>. (accessed: 22.10.2021).
- [5] Frederic Amant et al. “Endometrial cancer”. In: *The Lancet* 366.9484 (2005), pp. 491–505. ISSN: 0140-6736. DOI: [https://doi.org/10.1016/S0140-6736\(05\)67063-8](https://doi.org/10.1016/S0140-6736(05)67063-8).
- [6] Philippe Morice et al. “Endometrial cancer”. In: *The Lancet* 387 (10023 Mar. 2016), pp. 1094–1108. ISSN: 0140-6736. DOI: 10.1016/S0140-6736(15)00130-0.
- [7] Martin Koskas et al. “Cancer of the corpus uteri: 2021 update”. In: *International Journal of Gynecology Obstetrics* 155 (S1 Oct. 2021), pp. 45–60. ISSN: 1879-3479. DOI: 10.1002/IJGO.13866.
- [8] Cancer research UK. *Stages of womb cancer*. URL: <https://www.cancerresearchuk.org/about-cancer/womb-cancer/stages>. (accessed: 28.11.2022).
- [9] Kouji Banno et al. “Biomarkers in endometrial cancer: Possible clinical applications (Review)”. In: *Oncology Letters* 3 (6 June 2012), p. 1175. ISSN: 17921074. DOI: 10.3892/OL.2012.654.
- [10] Ingrid S Haldorsen and Helga B Salvesen. “What Is the Best Preoperative Imaging for Endometrial Cancer?” In: (2016). DOI: 10.1007/s11912-016-0506-0.
- [11] I. S. Haldorsen et al. “Increased microvascular proliferation is negatively correlated to tumour blood flow and is associated with unfavourable outcome in endometrial carcinomas”. In: *British Journal of Cancer* 110 (1 2014), pp. 107–114. ISSN: 00070920. DOI: 10.1038/bjc.2013.694.
- [12] Kristine E. Fasmer et al. “Preoperative quantitative dynamic contrast-enhanced MRI and diffusion-weighted imaging predict aggressive disease in endometrial cancer”. In: *Acta Radiologica* 59 (8 Aug. 2018), pp. 1010–1017. ISSN: 16000455. DOI: 10.1177/0284185117740932.

- [13] Zhijun Ye et al. “Endometrial carcinoma: use of tracer kinetic modeling of dynamic contrast-enhanced MRI for preoperative risk assessment”. In: *Cancer Imaging* 22 (1 Dec. 2022), pp. 1–11. ISSN: 14707330. DOI: 10.1186/S40644-022-00452-8/TABLES/4.
- [14] Paul S Tofts et al. *Estimating Kinetic Parameters From Dynamic Contrast-Enhanced T₁-Weighted MRI of a Diffusible Tracer: Standardized Quantities and Symbols*. 1999, pp. 223–232.
- [15] Jeremy Chen, Jianhua Yao, and David Thomasson. “Automatic Determination of Arterial Input Function for Dynamic Contrast Enhanced MRI in Tumor Assessment”. In: *Medical image computing and computer-assisted intervention : MICCAI ... International Conference on Medical Image Computing and Computer-Assisted Intervention* 11 (Pt 1 2008), p. 594. ISSN: 03029743. DOI: 10.1007/978-3-540-85988-8_71.
- [16] Eli Renate Grüner. *Compendium PHYS212 Medical Physics and Technology, version 1.0*. Department of Physics and Technology, Faculty of Mathematics and Natural Sciences, University of Bergen, Bergen, Norway. 2012.
- [17] Yaron Gordon et al. “Dynamic contrast-enhanced magnetic resonance imaging: fundamentals and application to the evaluation of the peripheral perfusion”. In: *Cardiovascular Diagnosis and Therapy* 4 (2 Apr. 2014), p. 147. ISSN: 2223-3652. DOI: 10.3978/J.ISSN.2223-3652.2014.03.01.
- [18] Paul S Tofts and Geoff J M Parker. “DCE-MRI: acquisition and analysis techniques”. In: ed. by Peter B. Barker, Xavier Golay, and Greg Zaharchuk. Cambridge University Press, 2013. Chap. 4, pp. 58–74.
- [19] Erlend Hodneland et al. “Automated segmentation of endometrial cancer on MR images using deep learning”. In: *Scientific Reports* 2021 11:1 11 (1 Jan. 2021), pp. 1–8. ISSN: 2045-2322. DOI: 10.1038/s41598-020-80068-9.
- [20] William J.D. Whiteley and Jonathan G. Hardman. “Pharmacokinetic analysis”. In: *Anaesthesia Intensive Care Medicine* 18 (9 Sept. 2017), pp. 455–457. ISSN: 1472-0299. DOI: 10.1016/J.MPAIC.2017.06.006.
- [21] Paul S. Tofts. *T₁ weighted DCE Imaging Concepts: Modelling, Acquisition and Analysis*. 2010. URL: http://paul-tofts-phd.org.uk/DCE-MRI_siemens.pdf. (accessed: 13.01.2022).
- [22] Steven P. Sourbron and David L. Buckley. “On the scope and interpretation of the Tofts models for DCE-MRI”. In: *Magnetic Resonance in Medicine* 66 (3 Sept. 2011), pp. 735–745. ISSN: 1522-2594. DOI: 10.1002/MRM.22861.
- [23] Questions and answers in MRI. *DCE Parameters: What quantitative parameters can be extracted from the DCE data?* URL: <https://mriquestions.com/dce-tissue-parameters.html#>. (accessed: 14.01.2022).
- [24] Jeroen Rouwkema, Nicolas C. Rivron, and Clemens A. van Blitterswijk. “Vascularization in tissue engineering”. In: *Trends in Biotechnology* 26.8 (2008), pp. 434–441. ISSN: 0167-7799. DOI: <https://doi.org/10.1016/j.tibtech.2008.04.009>.
- [25] Fahmi Khalifa et al. “Models and methods for analyzing DCE-MRI: A review”. In: *Medical Physics* 41 (12 2014). ISSN: 2473-4209. DOI: 10.1118/1.4898202.

- [26] Christian Tønnes et al. “Deterministic Arterial Input Function selection in DCE-MRI for automation of quantitative perfusion calculation of colorectal cancer”. In: *Magnetic Resonance Imaging* 75 (Jan. 2021), pp. 116–123. ISSN: 18735894. DOI: 10.1016/j.mri.2020.09.009.
- [27] Geoff J.M. Parker et al. “Experimentally-derived functional form for a population-averaged high-temporal-resolution arterial input function for dynamic contrast-enhanced MRI”. In: *Magnetic Resonance in Medicine* 56 (5 Nov. 2006), pp. 993–1000. ISSN: 1522-2594. DOI: 10.1002/MRM.21066.
- [28] The Medical Imaging Technology Association (MITA) a division of NEMA. *Key Concepts*. URL: <https://www.dicomstandard.org/concepts>. (accessed: 30.01.2023).
- [29] Arne Borthne. *PACS*. URL: <https://sml.snl.no/PACS>. (accessed: 19.01.2023).
- [30] Brent J. Liu and H.K. Huang. “13 - PACS and Medical Imaging Informatics for Filmless Hospitals”. In: *Biomedical Information Technology*. Ed. by David Dagan Feng. Biomedical Engineering. Burlington: Academic Press, 2008, pp. 279–305. ISBN: 978-0-12-373583-6. DOI: <https://doi.org/10.1016/B978-012373583-6.50017-7>.
- [31] Mona Alhajeri and Syed Ghulam Sarwar Shah. “Limitations in and Solutions for Improving the Functionality of Picture Archiving and Communication System: an Exploratory Study of PACS Professionals Perspectives”. In: (Sept. 2018). DOI: <https://doi.org/10.1007/s10278-018-0127-2>.
- [32] Sectra. *Sectra Radiology PACS and RIS*. URL: <https://medical.sectra.com/product/sectra-radiology-pacs-ris/>. (accessed:30.05.2023).
- [33] Paul A. Harris et al. “Research electronic data capture (REDCap)A metadata-driven methodology and workflow process for providing translational research informatics support”. In: *Journal of Biomedical Informatics* 42.2 (2009), pp. 377–381. ISSN: 1532-0464. DOI: <https://doi.org/10.1016/j.jbi.2008.08.010>.
- [34] Paul A. Harris et al. “The REDCap consortium: Building an international community of software platform partners”. In: *Journal of Biomedical Informatics* 95 (2019), p. 103208. ISSN: 1532-0464. DOI: <https://doi.org/10.1016/j.jbi.2019.103208>.
- [35] Hauke Bartsch. *A tool to create workflows for the research PACS*. URL: <https://github.com/mmiv-center/Research-Information-System/tree/master/components/Workflow-Image-AI>. (accessed:17.02.2023).
- [36] Davide Giavarina. “Understanding Bland Altman analysis”. In: *Biochimica Medica* 25 (2 2015), p. 141. ISSN: 13300962. DOI: 10.11613/BM.2015.015.
- [37] Are Hugo Pripp. “Pearsons eller Spearmans korrelasjonskoeffisienter”. In: *Tidsskrift for Den norske legeförening* 138 (8 May 2018). ISSN: 0029-2001. DOI: 10.4045/TIDSSKR.18.0042.
- [38] Patrick Schober and Lothar A. Schwarte. “Correlation Coefficients: Appropriate Use and Interpretation”. In: *Anesthesia and Analgesia* 126 (5 May 2018), pp. 1763–1768. ISSN: 15267598. DOI: 10.1213/ANE.0000000000002864.
- [39] Patrick Schober and Thomas R. Vetter. “Nonparametric Statistical Methods in Medical Research”. In: *Anesthesia and Analgesia* 131 (6 Dec. 2020), p. 1862. ISSN: 15267598. DOI: 10.1213/ANE.0000000000005101.

- [40] Frank Wilcoxon. “Individual Comparisons by Ranking Methods”. In: *Biometrics Bulletin* 1 (6 Dec. 1945), p. 80. ISSN: 00994987. DOI: 10.2307/3001968.
- [41] Mary L Mchugh. “The Chi-square test of independence”. In: *Biochemia Medica* 23 (2013), pp. 143–152. DOI: 10.11613/BM.2013.018.
- [42] Stian Lydersen, Morten Wang Fagerland, and Petter Laake. “Pearsons khikvadrattest”. In: *Tidsskrift for Den norske legeforening* 139 (12 Sept. 2019). ISSN: 0029-2001. DOI: 10.4045/TIDSSKR.18.0125.
- [43] Are Hugo Pripp. “Why the p-value is significant”. In: *Tidsskrift for Den norske legeforening* 135 (16 Sept. 2015), p. 1462. ISSN: 0029-2001. DOI: 10.4045/TIDSSKR.15.0493.
- [44] Steven Tenny and Ibrahim Abdelgawad. “Statistical Significance”. In: *Annual Review of Statistics and Its Application* 7 (Nov. 2022), pp. 1–10. ISSN: 2326831X. DOI: 10.1146/annurev-statistics-031219-041051.
- [45] Amrita Sil, Jayadev Betkerur, and NilayKanti Das. “P-Value Demystified”. In: *Indian Dermatology Online Journal* 10 (6 2019), p. 745. ISSN: 2229-5178. DOI: 10.4103/IDDJ.IDDJ_368_19.
- [46] Seong Ho Park, Jin Mo Goo, and Chan Hee Jo. “Receiver Operating Characteristic (ROC) Curve: Practical Review for Radiologists”. In: *Korean Journal of Radiology* 5 (1 Mar. 2004), pp. 11–18. ISSN: 1229-6929. DOI: 10.3348/KJR.2004.5.1.11.
- [47] Rajul Parikh et al. “Understanding and using sensitivity, specificity and predictive values”. In: *Indian Journal of Ophthalmology* 56 (1 2008), p. 45. ISSN: 03014738. DOI: 10.4103/0301-4738.37595.
- [48] Ingfrid S. Haldorsen et al. “Standard 1.5-T MRI of endometrial carcinomas: modest agreement between radiologists”. In: *European radiology* 22 (7 July 2012), pp. 1601–1611. ISSN: 1432-1084. DOI: 10.1007/S00330-012-2400-Y.
- [49] Guido Van Rossum and Fred L Drake Jr. *Python reference manual*. Centrum voor Wiskunde en Informatica Amsterdam, 1995.
- [50] Erling Andersen. “Imagedata: A Python library to handle medical image data in NumPy array subclass Series”. In: (2022). DOI: 10.21105/joss.04133.
- [51] Pauli Virtanen et al. “SciPy 1.0: Fundamental Algorithms for Scientific Computing in Python”. In: *Nature Methods* 17 (2020), pp. 261–272. DOI: 10.1038/s41592-019-0686-2.
- [52] Erik Hanson et al. “Workflow sensitivity of post-processing methods in renal DCE-MRI”. In: *Magnetic Resonance Imaging* 42 (Oct. 2017), pp. 60–68. ISSN: 0730-725X. DOI: 10.1016/J.MRI.2017.05.003.
- [53] F. Pedregosa et al. “Scikit-learn: Machine Learning in Python”. In: *Journal of Machine Learning Research* 12 (2011), pp. 2825–2830.
- [54] Mark Jenkinson et al. “Improved Optimization for the Robust and Accurate Linear Registration and Motion Correction of Brain Images”. In: *NeuroImage* 17.2 (2002), pp. 825–841. ISSN: 1053-8119. DOI: <https://doi.org/10.1006/nimg.2002.1132>.
- [55] Shengyu Fan et al. “An Automatic Estimation of Arterial Input Function Based on Multi-Stream 3D CNN”. In: *Frontiers in Neuroinformatics* 13 (July 2019), p. 49. ISSN: 16625196. DOI: 10.3389/FNINF.2019.00049/BIBTEX.